



Cosmological parameters from the comparison of peculiar velocities with predictions from the 2M++ density field

Jonathan Carrick,¹ Stephen J. Turnbull,¹ Guilhem Lavaux^{1,2,3,4,5★}
and Michael J. Hudson^{1,4★}

¹Department of Physics and Astronomy, University of Waterloo, Waterloo, ON N2L 3G1, Canada

²CNRS, UMR7095, Institut d'Astrophysique de Paris, F-75014 Paris, France

³Institut d'Astrophysique de Paris, Sorbonne Universités, UPMC Univ Paris 06, UMR7095, F-75014 Paris, France

⁴Perimeter Institute for Theoretical Physics, 31 Caroline St. N., Waterloo, ON N2L 2Y5, Canada

⁵Canadian Institute for Theoretical Astrophysics, University of Toronto, 60 St. George Street, Toronto, ON M5S 1A7, Canada

Accepted 2015 March 11. Received 2015 March 10; in original form 2014 July 6

ABSTRACT

Peculiar velocity measurements are the only tool available in the low-redshift Universe for mapping the large-scale distribution of matter and can thus be used to constrain cosmology. Using redshifts from the 2M++ redshift compilation, we reconstruct the density of galaxies within $200 h^{-1}$ Mpc, allowing for the first time good sampling of important superclusters such as the Shapley Concentration. We compare the predicted peculiar velocities from 2M++ to Tully–Fisher and SNe peculiar velocities. We find a value of $\beta^* \equiv \Omega_m^{0.55}/b^* = 0.431 \pm 0.021$, suggesting $\Omega_m^{0.55}\sigma_{8,\text{lin}} = 0.401 \pm 0.024$, in good agreement with other probes. The predicted peculiar velocity of the Local Group arising from the 2M++ volume alone is $540 \pm 40 \text{ km s}^{-1}$, towards $l = 268^\circ \pm 4^\circ$, $b = 38^\circ \pm 6^\circ$, only 10° out of alignment with the cosmic microwave background dipole. To account for velocity contributions arising from sources outside the 2M++ volume, we fit simultaneously for β^* and an external bulk flow in our analysis. We find that an external bulk flow is preferred at the 5.1σ level, and the best fit has a velocity of $159 \pm 23 \text{ km s}^{-1}$ towards $l = 304^\circ \pm 11^\circ$, $b = 6^\circ \pm 13^\circ$. Finally, the predicted bulk flow of a $50 h^{-1}$ Mpc Gaussian-weighted volume centred on the Local Group is $230 \pm 30 \text{ km s}^{-1}$, in the direction $l = 293^\circ \pm 8^\circ$, $b = 14^\circ \pm 10^\circ$, in agreement with predictions from Λ cold dark matter.

Key words: Local Group – cosmic background radiation – cosmological parameters – large-scale structure of Universe.

1 INTRODUCTION

Peculiar velocities, i.e. deviations in the motions of galaxies from the Hubble flow, are valuable tools which probe the underlying distribution of dark matter, and are in fact the only practical means of doing so on large scales in the low-redshift Universe. They can be used to constrain the amplitude of matter density fluctuations on a range of scales. As the amplitude of such fluctuations are themselves cosmology dependent, the analysis of peculiar velocities provides a direct means of testing cosmological predictions.

In the current standard cosmological paradigm, the observed structure in the Universe is a result of gravitational instabilities which grew from density perturbations in an otherwise homogeneous background. This gravitational attraction of objects to surrounding structure results in peculiar motion, i.e. motion in addition to that resulting from the expansion of the Universe. Assuming only mass continuity and standard gravitation in an expanding universe,

in the linear regime where these fluctuations in density are small, i.e. $\delta(r) = (\rho - \bar{\rho})/\bar{\rho} \lesssim 1$, peculiar velocities are proportional to gravitational accelerations. This relation, as expressed in integral form, is as follows:

$$\mathbf{v}(\mathbf{r}) = \frac{f(\Omega_m)}{4\pi} \int d^3\mathbf{r}' \delta(\mathbf{r}') \frac{(\mathbf{r}' - \mathbf{r})}{|\mathbf{r}' - \mathbf{r}|^3}, \quad (1)$$

where $\mathbf{v}(\mathbf{r})$ is the peculiar velocity field, $\delta(\mathbf{r})$ is the mass density contrast, Ω_m is the cosmological density parameter, and where distances are measured in km s^{-1} (i.e. $r = HR$, where H is the Hubble parameter and R is the comoving distance in Mpc). The growth rate of density perturbations, $f(\Omega_m)$, is generally parametrized by Ω_m^γ , where $\gamma = 0.55$ for Λ cold dark matter (Λ CDM; Wang & Steinhardt 1998), which has recently been shown to be consistent with observations (Hudson & Turnbull 2012).

As the total matter density contrast cannot be observed, however, to make use of equation (1), an assumption must first be made as to how observed galaxies trace the underlying total matter. Assuming linear biasing holds on large scales, $\delta_g = b\delta$, where b is the linear bias factor, and where we have used the subscript ‘g’ when referring

* E-mail: lavaux@iap.fr (GL); mike.hudson@uwaterloo.ca (MJH)

to galaxies. Rewriting equation (1) in terms of the observable density contrast of galaxies in the nearby Universe, the proportionality factor between gravitational acceleration and peculiar velocity is then $\beta \equiv f/b$. Thus, if linear theory holds, by comparing measured peculiar velocities to those predicted by the distribution of galaxies in redshift surveys, one can constrain cosmological parameters through the measurement of β . Furthermore, under the assumption of linear biasing $\sigma_{8,g} = b\sigma_8$, where σ_8 is the root mean square density fluctuations on an $8 h^{-1}$ Mpc scale.

By measuring $\sigma_{8,g}$ directly from the redshift data, one can eliminate b and constrain the degenerate cosmological parameter combination $f\sigma_8 = \beta\sigma_{8,g}$. Using this method of velocity–velocity comparison, a number of recent studies have constrained this parameter combination (Pike & Hudson 2005; Davis et al. 2011; Branchini, Davis & Nusser 2012; Turnbull et al. 2012).

In addition to constraints placed on these parameters, when full sky surveys are used one can compute the velocity of the Local Group (hereafter LG) arising from the volume under consideration as predicted by linear theory. While it has long been assumed that the dipole in the cosmic microwave background (CMB) temperature map is a Doppler effect due to the Sun’s motion, this has only been proved recently, via the aberration of the CMB temperature anisotropies (Planck Collaboration XXVII 2014b). The motion of the Sun with respect to the Galaxy and of the Galaxy with respect to the barycentre of the LG are well known (e.g. Courteau & van den Bergh 1999), and when combined with the Sun’s motion with respect to the CMB (Hinshaw et al. 2009) allows a determination of the motion of the LG with respect to the CMB: $622 \pm 35 \text{ km s}^{-1}$ in the direction $l = 272^\circ \pm 3^\circ$, $b = 28^\circ \pm 5^\circ$. A deviation from the predicted value with that derived from the CMB dipole would presumably arise from sources beyond the survey and would thus have implications for large-scale structure. As the tidal field falls off as r^{-3} , to first order one can model additional velocity contributions to the LG arising from sources outside the survey volume as a dipole, with the magnitude of this dipole, or residual bulk flow, itself being a test for cosmological models. Past studies constraining cosmological parameters through comparison of predicted motion of the LG using linear theory and that derived from the CMB include Erdoğan et al. (2006a), and Bilicki et al. (2011). Recently such an analysis has been extended to the non-linear regime using a novel orbit-reconstruction algorithm to predict motions of nearby objects (Lavaux et al. 2010).

In addition to reconstructing the motion of the LG, one can explore the bulk motion of a large volume (typically the mean velocity of a $50 h^{-1}$ Mpc Gaussian-weighted window) as such motion probes the amplitude of matter power spectrum on large scales. As previous studies in this vein have found hints of excess power on large scales (cf. Watkins, Feldman & Hudson 2009), there has been interest in performing such analyses using peculiar velocity surveys (e.g. Turnbull et al. 2012; Hong et al. 2014).

In this work, we explore the methods used to self-consistently reconstruct the real space density field from redshift space while quantifying any biases intrinsic to this reconstruction method. We then use the recently constructed large full-sky 2M++ catalogue composed of 69 160 galaxy redshifts to measure β to high precision and constrain $f\sigma_8$. We further explore the growth of the LG’s dipole as predicted by linear perturbation theory arising from structures within 2M++, in addition to computing the bulk flow arising from this survey.

This paper is organized as follows: in Section 2, we briefly review construction of the 2M++ catalogue, we discuss accounting for incompleteness and functional dependence of galaxy bias on

luminosity when computing the density field, and we outline details of the reconstruction procedure. In Section 3, we explore the growth of the LG velocity amplitude arising from 2M++ as a function of survey depth. In Section 4, we discuss peculiar velocity surveys used, the methods used in comparing predicted velocities to measured velocities, as well as the results obtained from such analyses. We discuss and compare our results to those from recent literature in Section 5, and conclude in Section 6.

2 DENSITY FIELD RECONSTRUCTION

Redshift surveys measure positions of objects in redshift-space. As equation (1) requires real-space positions, we must first map observed redshifts to real-space distances. The observed redshift, z_{obs} , is related to cosmological redshift resulting from the expansion of the Universe, z_{cos} , and that resulting from peculiar velocities, z_{pec} , through

$$(1 + z_{\text{obs}}) = (1 + z_{\text{cos}})(1 + z_{\text{pec}}), \quad (2)$$

where for non-relativistic peculiar motions $cz_{\text{pec}} \simeq v_{\text{pec}}$. Note that in the above if z_{obs} is corrected to some frame of reference, such as the CMB, then v_{pec} is the peculiar velocity with respect to that frame. The comoving distance in the low-redshift Universe is then related to the cosmological redshift through

$$H_0 R \simeq c \left(z_{\text{cos}} - \frac{1 + q_0}{2} z_{\text{cos}}^2 \right) \quad (3)$$

(Peebles 1993), where R is the comoving distance, H_0 is the local value of the Hubble parameter, and where q_0 is the local value of the deceleration parameter, which is given by $q = \Omega_m/2 - \Omega_\Lambda$ for a flat Λ CDM Universe. As real-space positions are dependent on peculiar velocity predictions, which are themselves dependent on real-space positions, mapping redshifts to real-space must be done with care.

In this section, we discuss the 2M++ redshift catalogue, and outline the procedure used in reconstructing comoving positions of the galaxies therein. Section 2.1 reviews construction of 2M++, and in Section 2.2 we outline how galaxy weights were computed to account for the fact that 2M++ is magnitude limited. In Section 2.3, we briefly review the choice of smoothing kernel. We discuss the procedure used to normalize the smoothed density field to the same effective bias in Section 2.4. In Section 2.5, we outline the iterative scheme used to recover real-space positions from redshift-space, and in Section 2.6 we take a cosmographic tour through the recovered density field.

2.1 2M++ redshift compilation

The integral in equation (1) is over all space. In reconstructing the velocity field of the local Universe, therefore, clearly one would like a redshift survey that is very deep and as close to all-sky as possible. Two such catalogues which have been used extensively in the past include the sparsely sampled *IRAS* Point Source Catalogue Redshift Survey (PSCz; Saunders et al. 2000), and more recently, the shallower but more densely sampled Two-Micron All-Sky Redshift Survey (2MRS; Huchra et al. 2012). In this work, we use a superset of 2MRS, dubbed 2M++, constructed by Lavaux & Hudson (2011). This sample has greater depth than 2MRS, and superior sampling than PSCz. The photometry is from the Two-Micron-All-Sky-Survey (2MASS) Extended Source catalogue, (2MASS-XSC; Skrutskie et al. 2006), an all-sky survey in the J , H and K_s bands. Redshifts in the K_s band of the 2MASS Redshift Survey

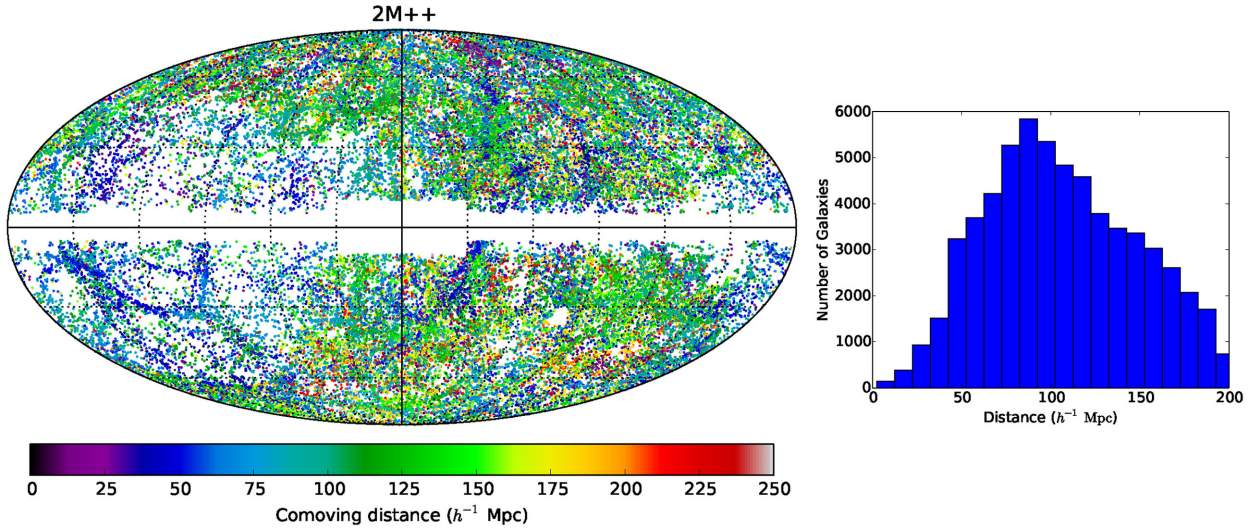


Figure 1. Left: all galaxies in 2M++ with measured redshifts; blue galaxies are nearest, red are farthest. The 2MRS region ($K_{2M++} \leq 11.5$) with lower density of galaxies is apparent. The Galactic Centre is in the centre of the plot, and Galactic longitude increases to the left. Right: histogram of galaxies in catalogue as a function of distance (bin width of $10 h^{-1}$ Mpc).

(2MRS) are supplemented by those from the Sloan Digital Sky Survey Data Release Seven (SDSS-DR7; Abazajian et al. 2009), and the Six-Degree-Field Galaxy Redshift Survey Data Release Three (6dFGRS; Jones et al. 2009). Data from SDSS were matched to that of 2MASS-XSC using the NYU-VAGC catalogue (Blanton et al. 2005). As 2M++ draws from multiple surveys, galaxy magnitudes from all sources were first recomputed by measuring the apparent magnitude in the K_s band within a circular isophote at $20 \text{ mag arcsec}^{-2}$. Following a prescription described in Lavaux & Hudson (2011), magnitudes were then corrected for Galactic extinction, cosmological surface brightness dimming and stellar evolution. After corrections the sample was limited to $K_{2M++} \leq 11.5$ in regions not covered by 6dFGRS or SDSS, and limited to $K_{2M++} \leq 12.5$ elsewhere.

Other relevant corrections which were made to this catalogue include accounting for incompleteness due to fibre-collisions in 6dF and SDSS, as well as treatment of the *zone of avoidance* (ZoA). Incompleteness due to fibre-collisions was treated by cloning redshifts of nearby galaxies within each survey region as described in Lavaux & Hudson (2011).

In treating the ZoA, for Galactic longitudes in the range $[30^\circ, 330^\circ]$, lower latitudes ($|b| < 5^\circ$) were first masked and then cloned with the redshifts from 2MRS in an equal-area strip just above the missing northern ($0^\circ < b < 5^\circ$) Galactic strip, and, for the negative Galactic latitudes in the south, a strip below that was cloned. Near the Galactic Centre, for longitudes in the range $[-30^\circ, 30^\circ]$, the wider Galactic latitude strip $|b| < 10^\circ$ was filled with the redshifts from 6dFGRS in a similar way. A histogram of distances is shown in Fig. 1.

2.2 Luminosity function and galaxy weights

Before using the catalogue to construct the density field, we must first account for survey incompleteness. In this section, we provide a summary of the method used to obtain the luminosity function fit to the catalogue; this luminosity function is in turn used in the weighting scheme employed to account for incompleteness. For a complete description of these calculations as applied to this catalogue see Lavaux & Hudson (2011). The luminosity function used

to characterize the data set is the Schechter function (1976), which when written in terms of absolute magnitudes is given by

$$\Phi(M) = 0.4 \log(10) n^* 10^{0.4(1+\alpha)(M^*-M)} \exp(-10^{0.4(M^*-M)}), \quad (4)$$

where n^* is the density normalization, M^* is the absolute magnitude break, and α is additional power-law parameter to be determined. Schechter function parameters are computed using likelihood formalism, where the product of all conditional probabilities of observing galaxies intrinsic magnitudes is maximized given their redshifts, Schechter parameter values, and survey completeness at their specified angular positions and distances.

Before computing weights we first discuss the different ways by which we can model the galaxy density contrast. As we cannot compute the mass density contrast of observed galaxies directly, we must use either the number-density of galaxies, or their luminosity-density in computing δ_g . In the context of linear biasing, our goal is to create a galaxy density contrast field which most closely traces the underlying total mass density contrast. Although luminosity-density may be a better proxy for stellar mass, and thus for the underlying mass distribution of dark matter, we will consider both schemes in this work.

To account for incompleteness, galaxies are weighted according to a common prescription similar to that of Davis & Huchra (1982). In the case of a number-density scheme, observed galaxies are weighted to account for the number of galaxies not observed at a given distance due to the magnitude limit of the survey. When using the galaxy number-density for a single homogeneous redshift survey, galaxies are weighted by

$$w^N(r) = \frac{N_{\text{average}}}{N_{\text{observed}}(r)} = \frac{\int_{L_{\min}}^{\infty} \Phi(L) dL}{\int_{4\pi r^2 f_{\min}}^{\infty} \Phi(L) dL}, \quad (5)$$

when $4\pi d_L^2 f_{\min} > L_{\min}$, and unity otherwise. The flux limit, f_{\min} , corresponds to a K_s band apparent magnitude limit of 11.5 for galaxies drawn from 2MRS and 12.5 otherwise. The luminosity L_{\min} used above corresponds to a K_s band absolute magnitude of -20 . Computed weights used in this work additionally account for the inhomogeneous incompleteness of 2M++ and a complete

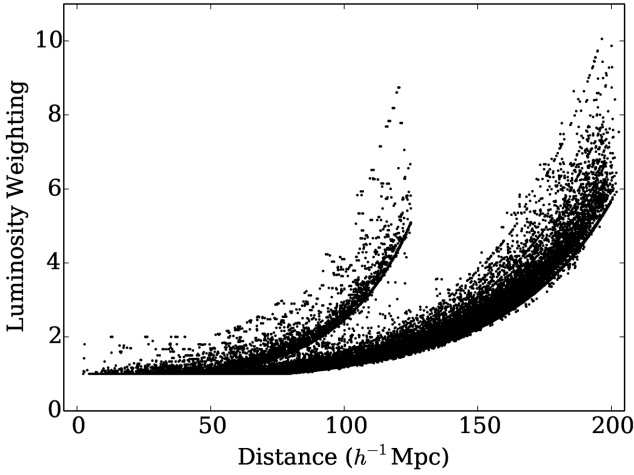


Figure 2. Computed luminosity weights obtained from the procedure outlined in Section 2.2. As 2MRS is magnitude limited to $K_s < 11.5$, weights rise more sharply than for SDSS and 6dF galaxies which are magnitude limited to $K_s < 12.5$. The scatter in the weights at a given distance arises from varying levels of redshift completeness across the sky.

description of their determination can be found in Lavaux & Hudson (2011).

In this paper, by default, we will use luminosity-density to compute the galaxy density contrast. The weight assigned to each galaxy's luminosity is again based on the fraction of the total luminosity expected, given the magnitude limit of the survey, to the luminosity one expects to observe at a given distance. Thus, for a single homogeneous redshift survey, galaxy luminosities are weighted by

$$w^L(r) = \frac{L_{\text{average}}}{L_{\text{observed}}(r)} = \frac{\int_{L_{\min}}^{\infty} L \Phi(L) dL}{\int_{4\pi r^2 f_{\min}}^{\infty} L \Phi(L) dL}. \quad (6)$$

The calculated luminosity weights obtained for the best values of cosmological parameters are shown in Fig. 2.

2.3 Smoothing

In order to use equation (1), the density field must first be sufficiently smooth for linear perturbation theory to apply. The optimal scale on which to smooth the data was determined by comparing velocities from an N -body simulation to predictions obtained through linear theory using different smoothing lengths. Smoothing the density contrast with a $4 h^{-1}$ Mpc Gaussian was found to be the best compromise in minimizing the scatter in predicted velocities versus simulation velocities, while simultaneously returning an unbiased slope in the comparison of observed nonlinear velocities (from the simulation) with the linear theory predictions from a smoothed, reconstructed density field of haloes. These comparisons are discussed in greater detail in Appendix A.

2.4 Accounting for magnitude dependence of galaxy-matter bias

For magnitude limited surveys such as 2M++, the mean luminosity of observed galaxies increases with depth. As galaxy-matter bias has been found to increase with luminosity, this means that objects observed at higher redshift are on average more biased than those observed nearby. In this section, we account for this effect by rescaling the density field to the same effective bias. We do so

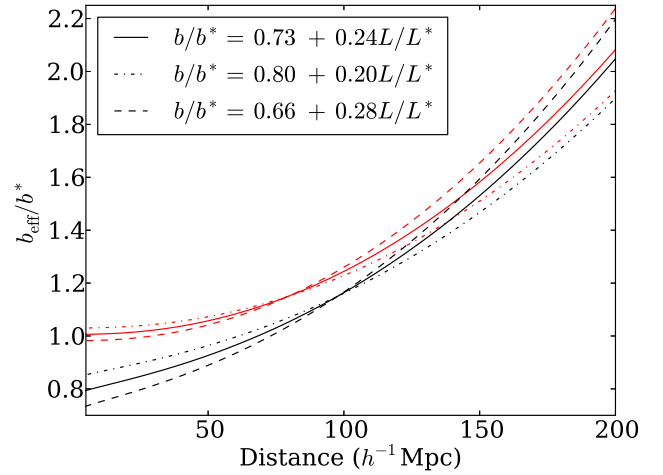


Figure 3. Number-weighted (lower) and luminosity-weighted (upper) effective bias as a function of distance for the most significant 1σ deviation of parameters from the scaling relation $b/b^* = (0.73 \pm 0.07) + (0.24 \pm 0.04)L/L^*$. Plots are obtained using the parameter values $\alpha = -0.85$ and $M^* = -23.25$ for the Schechter luminosity function.

using the bias model of Westover (2007) in which bias is a function of luminosity. By comparing the correlation function of 2MASS volume-limited subsamples, converting the binned absolute magnitude to a luminosity and defining $b/b^* = (\xi(s)/\xi_{\text{fid}}(s))^{1/2}$, Westover (2007) found $b/b^* = (0.73 \pm 0.07) + (0.24 \pm 0.04)L/L^*$, where b^* is the bias of an L^* galaxy. This result is consistent with that of Norberg et al. (2001) and Tegmark et al. (2002), who did similar analyses using projected correlation functions of 2dFGRS and the SDSS power spectrum, respectively.

Since bias is a function of luminosity, this means that a naive computation of the density field using a magnitude limited survey would lead to a larger effective bias at larger distances. As our end goal is to compare predicted velocities with measured velocities and determine f/b , we must first correct the density contrast field by normalizing the field to the same effective bias. The effective number-weighted bias is computed as follows:

$$b_{\text{eff}}^N(r) = \frac{\int_{4\pi r^2 f_{\min}}^{\infty} b(L) \Phi(L) dL}{\int_{4\pi r^2 f_{\min}}^{\infty} \Phi(L) dL} = \psi^N(r) b^*. \quad (7)$$

Using a luminosity-weighting scheme in computing the density contrast, the effective luminosity-weighted bias is given by

$$b_{\text{eff}}^L(r) = \frac{\int_{4\pi r^2 f_{\min}}^{\infty} b(L) L \Phi(L) dL}{\int_{4\pi r^2 f_{\min}}^{\infty} L \Phi(L) dL} = \psi^L(r) b^*. \quad (8)$$

Using the functional form of $b(L)$ quoted above from Westover (2007), this normalization procedure was applied to the 2M++ density contrast fields. Both the number-weighted and luminosity-weighted effective bias for $\alpha = -0.85$, $M^* = -23.25$, and a magnitude limit of 12.5 are shown in Fig. 3. We can then rewrite equation (1) as

$$\mathbf{v}(\mathbf{r}) = \frac{\beta^*}{4\pi} \int d^3\mathbf{r}' \delta_g^*(\mathbf{r}') \frac{(\mathbf{r}' - \mathbf{r})}{|\mathbf{r}' - \mathbf{r}|^3}, \quad (9)$$

where we have defined $\beta^* \equiv f(\Omega)/b^*$, and $\delta_g^*(\mathbf{r}) \equiv b^* \delta(\mathbf{r}) = \delta_g(\mathbf{r})/\psi(\mathbf{r})$.

2.5 Reconstruction procedure

The weighted galaxies from 2M++ have measured redshifts cz , and not precise distances r . However, application of (1) requires distances as opposed to redshifts. We refer to the inverse problem of determining the positions from redshifts as ‘reconstruction’. Reconstruction was accomplished via an iterative procedure modelled on that of Yahil et al. (1991). Objects were first grouped using the ‘Friends-of-friends’ algorithm (Huchra & Geller 1982), and then placed at the mean of their group redshift distance to suppress the ‘Fingers-of-God’ effect. Gravity was then ‘adiabatically’ turned on by increasing $\beta^* \equiv f(\Omega_m)/b^*$ from 0 to 1 in steps of 0.01. The reconstruction took place in the LG frame, and on each iteration the following steps were taken.

(i) A Schechter luminosity function is fitted to the data using the likelihood formalism discussed in Section 2.2. The LF is in turn used to compute either the luminosity or number weights following the procedure discussed in Section 2.2.

(ii) Galaxies from 2MRS with distances greater than $125 h^{-1}$ Mpc are assigned a weight of zero. Galaxy properties, including newly computed weights are then cloned to account for incompleteness and fill the ZoA as described in Section 2.1.

(iii) Number weighted galaxies or their weighted luminosities within $200 h^{-1}$ Mpc are then placed on a grid.

(iv) The density contrast field is then computed and normalized to the same bias, b^* , as described in Section 2.4. The field is in turn smoothed with a Gaussian kernel of width $4 h^{-1}$ Mpc.

(v) Using equation (9), the density contrast field is then used to obtain predicted peculiar velocities for all objects in the catalogue.

(vi) In conjunction with measured redshifts, predicted peculiar velocities projected on to the line of sight (LOS) are then used to predict comoving distances using equations (2) and (3).

(vii) The previous five predictions for a galaxy’s distance are then averaged to suppress oscillations arising from triple valued regions, i.e. regions of high-density near which there are multiple solutions for distance given redshift (discussed further in Appendix B). The averaged distance is in turn assigned to the galaxy and used to recompute the galaxy’s absolute magnitude. Computed distances and magnitudes are then used in the subsequent iteration.

Catalogues containing updated distances, luminosities and weights were saved at each iteration (corresponding to increasing values of β) in addition to the computed density and velocity fields.

It should be noted that this iterative reconstruction procedure was found to be unbiased in determining the best-fitting value of β^* when the full analysis was run on an N -body simulation using a Λ CDM cosmology (see Appendix A for more details).

2.6 Cosmography

Fig. 4 shows the luminosity-weighted density field of the Supergalactic Plane for $\beta^* = 0.43$, smoothed with a $4 h^{-1}$ Mpc Gaussian kernel. The incomplete coverage due to the lower magnitude limit of 2MRS is clearly visible in this figure beyond $SGX \simeq 125 h^{-1}$ Mpc. The most prominent overdensity in this plane is the Shapley Concentration located at $(SGX, SGY) \simeq (-125, 75) h^{-1}$ Mpc. Other notable structures in Fig. 4 include the Virgo Supercluster directly above the LG, the Hydra–Centaurus Supercluster at $(-40, 20) h^{-1}$ Mpc, and the Perseus–Pisces Supercluster $(40, -30) h^{-1}$ Mpc. Additional slices through SGZ are shown in Fig. 5, though smoothed on a $7 h^{-1}$ Mpc scale to enhance the contrast of large overdensities. For instance, Horologium–Reticulum Supercluster can be readily ob-

served at $SGZ \simeq -112 h^{-1}$ Mpc, $SGX \simeq -70 h^{-1}$ Mpc, $SGY \simeq -140 h^{-1}$ Mpc. The supergalactic plane is also shown with this smoothing for comparison.

3 2M++ PREDICTED PECULIAR VELOCITY OF THE LOCAL GROUP

The velocity of the LG as predicted by linear perturbation theory for an ideal distance-limited catalogue is given by

$$\mathbf{v}_{\text{LG}} = \frac{\beta}{4\pi} \int_0^{R_{\text{max}}} d^3 \mathbf{r}' \delta_{\mathbf{g}}(\mathbf{r}') \frac{\mathbf{r}'}{r'^3} + \mathbf{V}_{\text{ext}}, \quad (10)$$

where \mathbf{V}_{ext} encapsulates contributions from beyond R_{max} , and to first order, can be approximated as a dipole, or ‘residual’ bulk flow. For a realistic flux-limited catalogue, we do not detect a continuous distribution of matter but a finite number of galaxies. As a result, our estimate of the velocity of the LG using 2M++ is subject to shot noise. To estimate the effect of shot noise on our predicted motion of the LG, we computed the standard deviation in each of the components of 500 bootstrap samples. The shot noise in the amplitude of the LG’s motion from this analysis was found to be 56 km s^{-1} .

Under the assumption that the observed CMB dipole arises from the motion of the LG, there has been much debate as to the structures sourcing this motion. Most recent work has made use of 2MASS-XSC or 2MRS in reconstructing the motion of the LG, and there has yet to be consensus on the distance at which the LG’s motion coincides with that derived from the CMB. Erdoğdu et al. (2006b) argue that more than 70 percent of the LG’s motion results from structures within $50 h^{-1}$ Mpc, such as Hydra–Centaurus Supercluster. While others argue for convergence at distances greater than $\sim 120 h^{-1}$ Mpc such as Lavaux et al. (2010) using Monge–Ampère–Kantorovich orbit-reconstruction method, or Bilicki et al. (2011), who explored the convergence of the 2MASS dipole moment of the angular distribution of galaxies as a function of the limiting flux of the sample. As 2M++ is a superset of 2MRS and contains redshift measurements up to a magnitude limit of $K_s = 12.5$, these data are well suited to examine the influence of structures beyond $120 h^{-1}$ Mpc on the velocity of the LG.

Using density fields for different values of β^* that were obtained throughout the iteration procedure discussed in Section 2.5, the velocity field of increasingly larger concentric spheres centred on the LG was computed. The direction and amplitude of the LG velocity as a function of distance for different values of β^* was then obtained. The amplitude of the LG velocity as predicted by 2M++ for different values of β^* is shown in Fig. 6(a). The expected agreement between predictions using linear perturbation theory for a survey of a certain depth with values derived from the CMB is plotted for comparison. This conditional probability assumes a Λ CDM *Wilkinson Microwave Anisotropy Probe 9* (WMAP9) cosmology. A derivation of this conditional velocity can be found in appendix A of Lavaux et al. (2010), and is based on Lahav, Kaiser & Hoffman (1990). The convergence of the direction of LG velocity with that derived from the CMB ($l = 272^\circ \pm 3^\circ$, $b = 28^\circ \pm 5^\circ$) is plotted in Fig. 6(b). For our best-fitting value of $\beta^* = 0.43$ from Section 4 below, the misalignment is 10° . This misalignment angle is significantly better than those found by past studies using the shallower 2MRS, such as the 21° misalignment found by Erdoğdu et al. (2006a), 19° found by Bilicki et al. (2011), or the $\sim 45^\circ$ misalignment found by Lavaux et al. (2010).

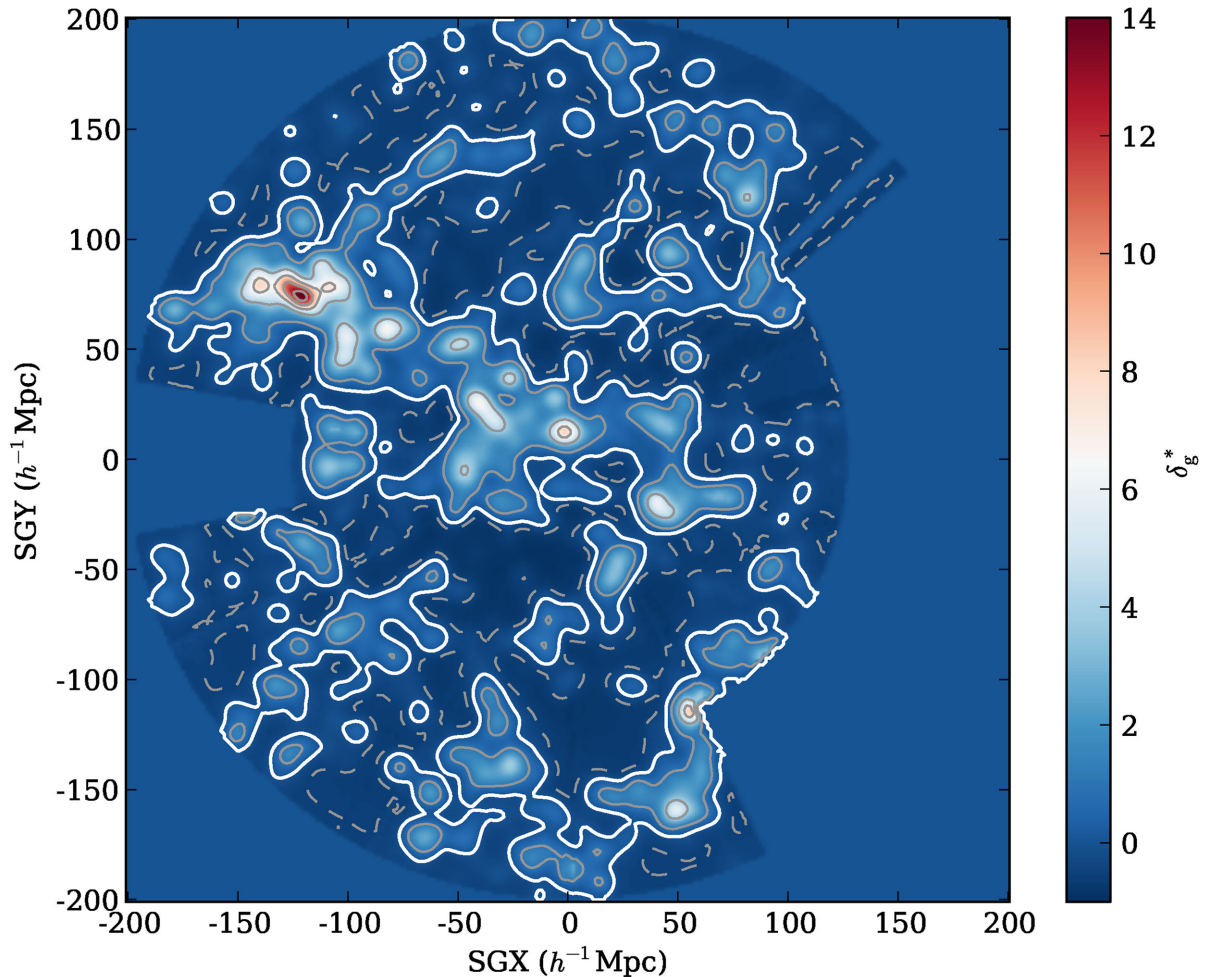


Figure 4. The Supergalactic Plane ($SGZ = 0$) of the 2M++ luminosity-weighted galaxy density contrast field, reconstructed with $\beta^* = 0.43$ smoothed with a Gaussian kernel of radius $4 h^{-1}$ Mpc. The dashed contour is $\delta_g^* = -0.5$, the bold white contour is $\delta_g^* = 0$, and successive contours thereafter increase from 1 upwards in steps of 3. The Galactic plane runs roughly along the $SGY=0$ axis. The Shapley Concentration is located at $(SGX, SGY) \simeq (-125, 75) h^{-1}$ Mpc, the Virgo Supercluster directly above the LG, the Hydra–Centaurus Supercluster at $(-40, 20) h^{-1}$ Mpc, and the Perseus–Pisces Supercluster is at $(40, -30) h^{-1}$ Mpc. The density field is shallower at positive SGX because this region is only covered by the 2MRS, whereas the rest of the plane is covered by the deeper 6dFGS and SDSS.

4 PECULIAR VELOCITY COMPARISONS

In principle, it is possible to constrain cosmological parameters by comparing the growth of predicted motion of the LG with its observed motion. This is difficult in practice because one expects contributions from sources beyond the survey limit, which we have modelled here as a residual dipole V_{ext} . There is therefore a degeneracy between β^* and V_{ext} parameters appearing in equation (10). Very early studies of the growth of the LG gravity dipole observed the flatness at large radii from data similar to that shown in Fig. 6, therefore assumed that V_{ext} was negligible, and hence solved for β^* . This procedure, however, leads to a value of β which is biased high, since V_{ext} and the integral in (10) are correlated. An alternative approach is to constrain V_{ext} by assuming a cosmological model of density fluctuations, but this then makes the exercise model dependent.

A better approach is to break the degeneracy by measuring peculiar velocities of galaxies or groups other than the LG. In this section, we discuss comparisons between the predicted and observed motions of two samples of galaxies, derived from the Tully–Fisher (TF) relation and from Type Ia supernovae.

4.1 Peculiar velocity surveys

4.1.1 SFI++

SFI++ (Springob et al. 2007) builds primarily on Spiral Cluster *I*-band (SCI) and Spiral Field *I*-band (SFI) samples and uses a mixture of 21-cm line profile widths and optical rotation curves in determining the *I*-band TF relation from a subset of 807 galaxies in the fields of 31 clusters and groups (Masters et al. 2006). From the derived TF relation, they in turn determine the peculiar velocities of 5780 galaxies. Upon removing galaxies without high-quality width measurements and those that are located beyond the volume covered by 2M++, SFI++ can be divided in to two subsets of 2583 field galaxies and 735 galaxy groups.

As noted by Davis et al. (2011), the SFI++ TF relation has a kink in the faint end ($M > -20$), and an asymmetric distribution of outliers about the expected velocity width parameter $\eta \equiv \log(W) - 2.5$ (Springob et al. 2007). As we will be fitting for the inverse TF relation, we will account for the outliers and deviation from linearity of the relation by excluding galaxies with redshift-distance magnitudes fainter than -20 . We then iteratively compute the TF

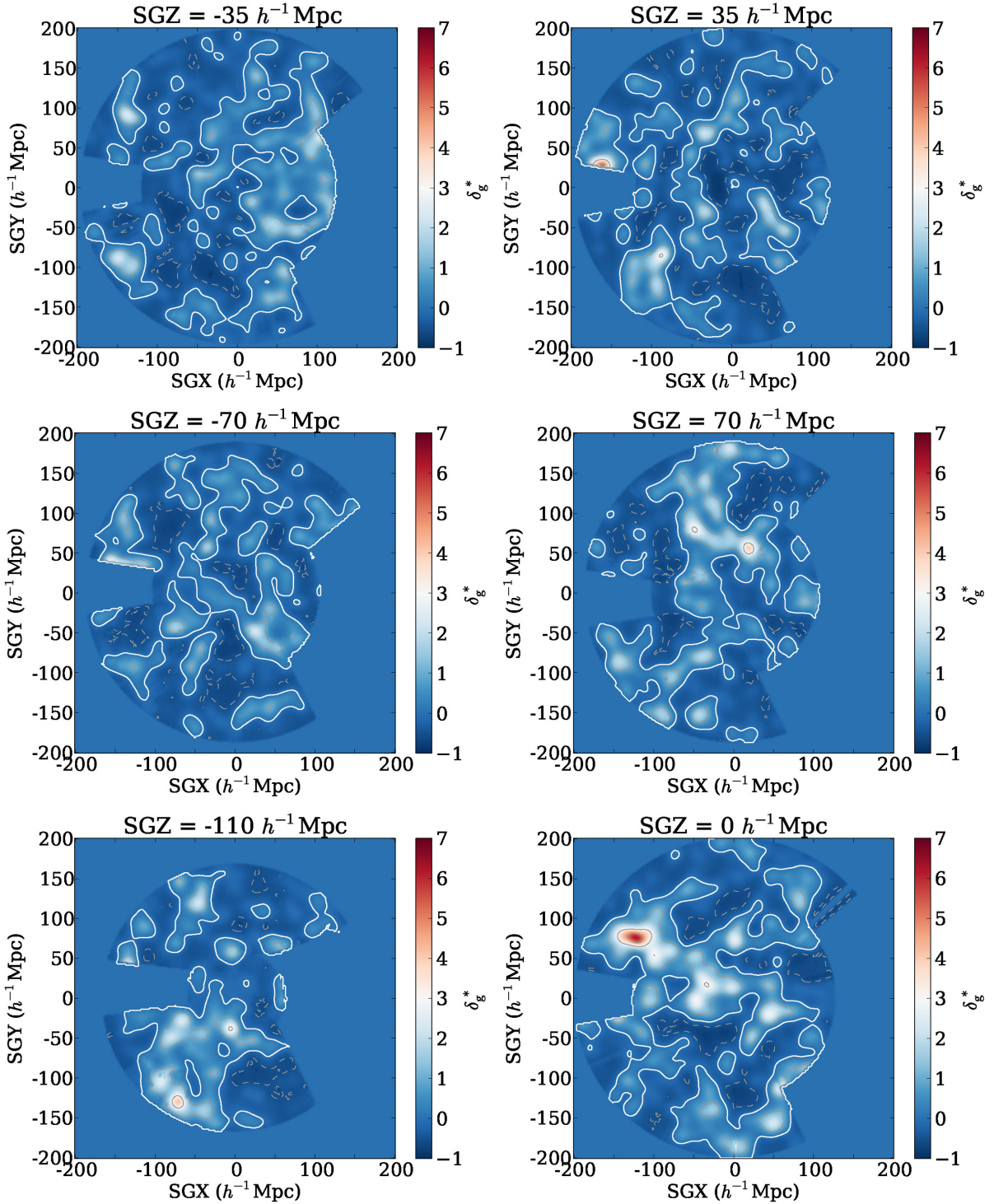


Figure 5. The 2M++ density field at various slices of SGZ. The density field was smoothed with a $7 h^{-1} \text{ Mpc}$ Gaussian kernel. The $\text{SGZ} = -110 h^{-1} \text{ Mpc}$ panel shows the Horologium-Reticulum supercluster. The dashed contour is $\delta_g^* = -0.5$, the bold white contour is $\delta_g^* = 0$, and successive contours thereafter increase from 1 upwards in steps of 2.

relation parameters and remove those with a velocity width that deviates by more than 0.2 in η (3.8σ) from the relation, until derived parameter values converge. Selection on both magnitude and velocity width resulted in the rejection of 503 field galaxies and 137 galaxy groups. Furthermore, when comparing predicted velocities from 2M++ with those from SFI++, the remaining objects

which were found to differ by more than 3.5σ with all velocity fields obtained through the reconstruction procedure were rejected (0.6 per cent). The final sample was composed of 2067 field galaxies and 595 galaxy groups. The typical or characteristic depth of the sample can be quantified by a weighted mean distance, where the weights are the inverse square of the uncertainties. This yields

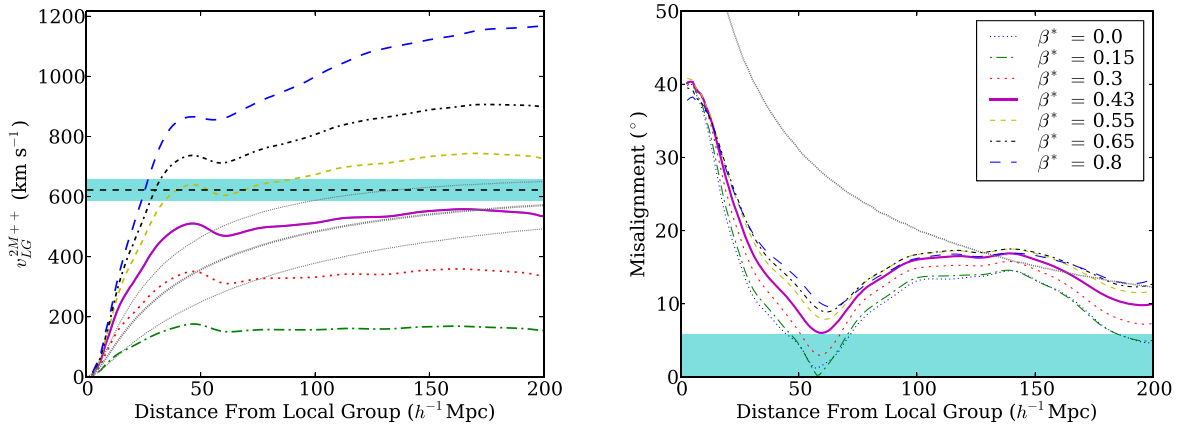


Figure 6. Left: growth of LG velocity amplitude as predicted by linear perturbation theory for successively larger concentric spheres. The non-monotonic curves correspond to the 2M++ predicted growth of the LG amplitude for different values of β^* as indicated in the legend. The solid purple curve is for our best-fitting value $\beta^* = 0.43$. The smooth thick grey line corresponds to the expected velocity amplitude for a survey of a depth indicated by the x-axis in a ΛCDM WMAP9 cosmology. The thin grey lines indicate the 68 per cent uncertainties due to cosmic variance. The shaded cyan band corresponds to the velocity of the LG and its 68 per cent uncertainties as inferred from the CMB dipole. Right: the misalignment of the LG predicted direction of the velocity arising from 2M++ with that derived from the CMB ($l = 272^\circ$, $b = 28^\circ$). The smooth grey curve indicates the 68 per cent uncertainty on the alignment expected in the WMAP9 cosmology.

depths of $42 h^{-1} \text{Mpc}$ and $25 h^{-1} \text{Mpc}$ for field and group samples, respectively.

For the TF relation, we will perform the fit two different ways. The first is a direct maximum-likelihood fit to the observed linewidths: the VELMOD method of Willick et al. (1997), as described in Section 4.2.1 below. The second method uses the estimated distances as given by Springob et al. (2007), but corrected for the fact that their peculiar velocities were obtained under the assumption that $cz_{\text{obs}} = H_0 R + v_{\text{pec}}$. Specifically, we use the analytic relation from equation (2) to obtain velocities from measured positions.

4.1.2 First Amendment Supernovae

The First Amendment (A1) catalogue Type Ia Supernovae (SNe) data sets were compiled by Turnbull et al. (2012). A1 is composed of SNe within $200 h^{-1} \text{Mpc}$ and draws 34 SNe from Jha, Riess & Kirshner (2007), 185 from Hicken et al. (2009) and 26 from Folatelli et al. (2010). Of these 245 SNe, 237 are within the volume spanned by 2M++, and have an uncertainty-weighted depth of $31 h^{-1} \text{Mpc}$.

4.2 Velocity–velocity comparisons

For the SFI++ subsets, we use the distances as determined in Springob et al. (2007) which have not been corrected for Malmquist bias. We similarly do not use Malmquist bias corrected A1 distances. Of the comparison methods discussed below, VELMOD is unaffected by inhomogeneous Malmquist bias, and accounts for homogeneous Malmquist bias in the likelihoods. The Forward Likelihood method discussed accounts for both homogeneous and inhomogeneous Malmquist bias in the likelihoods. The simple χ^2 comparison, however, neither accounts for homogeneous nor inhomogeneous Malmquist bias, and as such, the results yielded from this analysis are taken to be biased.

4.2.1 VELMOD

VELMOD is a rigorous maximum likelihood method first proposed and implemented by Willick et al. (1997) and described further

in Willick & Strauss (1998). It is a velocity–velocity comparison method used to fit for the TF relation parameters (zero-point, slope and scatter) while simultaneously fitting for β . VELMOD takes as inputs TF parameters, an object’s redshift and one of the observables (velocity-width or apparent magnitude), and maximizes the probability of observing one given the other. The strength of VELMOD analysis is that it neither assumes a one to one mapping from redshift space to real space (accounting for errors due to triple-valued regions), nor does it require calibration of the TF relation prior to its implementation.

Forward VELMOD uses the velocity-width to predict a galaxy’s apparent magnitude, whereas the inverse method uses the apparent magnitude to predict the velocity-width parameter. The forward method is strongly dependent on selection effects, and thus requires a well-modelled selection function. The inverse method, however, is much less sensitive to selection effects due to sample selection’s possible weak dependence on velocity-width. As the selection function of SFI++ is rather difficult to model accurately due to its being a compilation of various surveys with a range of selection criteria, we will make use of the inverse method in our analysis. This analysis assumes a TF relation of the form $\eta^0(M) = -b_{\text{inv}}^{-1}(M - a_{\text{inv}})$, where $\eta = \log_{10}(W) - 2.5$, $M = m - 5 \log(d_L(r))$ is the absolute magnitude, d_L is the luminosity distance, and where b_{inv} , a_{inv} and σ_η are the slope, intercept and rms scatter of the inverse relation, respectively.

The conditional probability of observing a measured velocity-width of a galaxy with an apparent magnitude, m , and an observed redshift, z , is given by

$$P(\eta|m, cz) = \frac{P(\eta, m, cz)}{\int_{-\infty}^{\infty} d\eta P(\eta, m, cz)}, \quad (11)$$

where

$$P(\eta, m, cz) = \int_0^\infty dr P(\eta, m|r) P(cz|r) r^2, \quad (12)$$

$$P(\eta, m|r) \propto \Phi(m - \mu(r)) S(m, \eta, r) \exp\left(-\frac{[\eta - \eta^0(m - \mu(r))]^2}{2\sigma_\eta^2}\right), \quad (13)$$

$$P(cz|r) = \frac{1}{\sqrt{2\pi\sigma_v^2}} \exp\left(-\frac{[cz - cz_{\text{pred}}]^2}{2\sigma_v^2}\right), \quad (14)$$

$$(1 + z_{\text{pred}}) = (1 + z_{\text{cos}}(r))(1 + \beta^* u(r)/c), \quad (15)$$

where $z_{\text{cos}}(r)$ is related to the comoving distance $r \equiv H_0 R$ through equation (3), $S(m, \eta, r)$ is the selection function, u is the radial predicted velocity scaled to $\beta^* = 1$, σ_v is the scatter in the actual velocity compared to the linear theory prediction, and where $\mu(r) \equiv 5 \log r$ is the distance modulus. We take $\sigma_v = 150 \text{ km s}^{-1}$ based on the tests discussed in Appendix A. We can then compute the product of the conditional probability $P(\eta|m, cz)$ over all galaxies and minimize the quantity

$$\mathcal{L}_{\text{IV}} = -2 \sum_i \ln P(\eta_i|m_i, cz_i) \quad (16)$$

for the parameters β^* , a_{inv} , b_{inv} , and the three components of \mathbf{V}_{ext} .

4.2.2 Forward likelihood

We use a maximum likelihood method first described in Pike & Hudson (2005) which was developed to compare peculiar velocities obtained through SNe surveys while accounting for triple-valued regions. In addition to constraining β^* and the three components of \mathbf{V}_{ext} this method can be used to constrain \tilde{h} , a nuisance parameter which permits a rescaling of published distances. The forward likelihood method maximizes the probability of a galaxy having its observed redshift

$$P(cz) = \int_0^\infty dr P(cz|r) P(r), \quad (17)$$

where

$$P(cz|r) = \frac{1}{\sqrt{2\pi\sigma_v^2}} \exp\left(-\frac{[cz - cz_{\text{pred}}]^2}{2\sigma_v^2}\right), \quad (18)$$

$$(1 + z_{\text{pred}}) = (1 + z_{\text{cos}}(r, \tilde{h}))(1 + \beta^* u(r)/c), \quad (19)$$

where z_{cos} is given through the relation

$$\tilde{h}r = cz_{\text{cos}} \left(1 - \frac{1 + q_0}{2} z_{\text{cos}}\right), \quad (20)$$

and where

$$P(r) \propto \exp\left(-\frac{[r - d]^2}{2\sigma_d^2}\right) [1 + \delta_g^*(r)], \quad (21)$$

d is the distance as determined by the peculiar velocity survey, and where σ_d is the uncertainty in the measured distance. The product of $P(cz)$ for all objects is then computed, from which the quantity $\mathcal{L}_{\text{FL}} = -2 \sum_i \ln P(cz_i)$ is minimized.

4.2.3 χ^2 minimization

In addition to the comparison method discussed above, we also perform a simple χ^2 minimization procedure to determine the best value of β^* and \mathbf{V}_{ext} . For this minimization procedure we compare the observed redshift of the object with the sum of its measured distance and predicted peculiar velocity at that distance, i.e.

$$\chi^2(\beta^*) = \sum_i \frac{(cz_i - cz_{\text{pred}})^2}{\sigma_{d_i}^2 + \sigma_v^2}, \quad (22)$$

Table 1. Summary of best-fitting values of β^* using different weighting schemes, methods of analysis and peculiar velocity data sets. Results obtained using luminosity weighting are indicated by (LW), whereas those obtained using number weighting are indicated by (NW). Unless explicitly indicated, all data sets were used for the method mentioned with the exception of Inverse VELMOD which used all individual galaxies from SFI++.

	β^*	$\chi^2/(\text{DOF})$
Forward likelihood (LW)		
A1	0.440 ± 0.023	–
SFI++ Galaxy Groups	0.429 ± 0.022	–
SFI++ Field Galaxies	0.423 ± 0.045	–
All	0.431 ± 0.021	–
Forward likelihood (NW)	0.439 ± 0.020	–
Inverse VELMOD (LW)	0.387 ± 0.048	–
χ^2 (LW)	0.444 ± 0.026	2194/2899
χ^2 (NW)	0.442 ± 0.028	2200/2899

Table 2. TF relation constants obtained through Inverse VELMOD analysis of SFI++ galaxies. Results listed are those obtained using a luminosity-weighting (LW) reconstruction scheme.

	a_{inv}	b_{inv}
Masters et al. (2006)	–20.881	–8.435
This study	-20.918 ± 0.012	-8.19 ± 0.06

where z_{pred} is given by equation (19). Note that this expression does not account for the effects of density inhomogeneities along the LOS. The recovered value of β^* is affected by inhomogeneous Malmquist bias and results from this method are thus expected to be biased high as a result. Nevertheless, the χ^2 statistic is useful to assess goodness-of-fit and so is included here.

4.3 Results

Key results obtained through velocity–velocity comparison methods discussed in Section 4.2 are summarized in Table 1. To determine the value of β^* at which \mathcal{L}_{FL} and χ^2 are minimized, a cubic function was fit to resultant data. Comparison of the TF relation constants (a_{inv} , b_{inv}) obtained to those found by Masters et al. (2006) are shown in Table 2. The best-fitting value for all parameters, including β^* and its errors were obtained from 500 bootstrap samples of both 2M++ and the peculiar velocity data sets. Through bootstrap analysis it was found that peculiar velocity data sets and 2M++ contributed essentially equal amounts to overall parameter errors. The value obtained for the best-fitting residual bulk flow, \mathbf{V}_{ext} , is given in Table 3 along with the bulk flow ($50 h^{-1} \text{ Mpc}$ Gaussian-weighted mean of the velocity field) and the predicted velocity of the LG arising from 2M++. A comparison of χ^2 with and without the residual bulk flow results in a difference of 34 for the 3 degrees of freedom, the residual bulk flow model is thus preferred at the 5.1σ level.

For a qualitative illustration of the agreement of predicted velocities arising from 2M++ with the published values from SFI++ and A1, we have plotted the projected LOS velocity within a 30° cone centred on the Shapley Supercluster and Hydra Supercluster in Fig. 7. These two structures were chosen as they lie in approximately the same direction as \mathbf{V}_{ext} . From this figure, it is

Table 3. The bulk flow and motion of the LG arising from 2M++ for our best value of $\beta^* = 0.43$. The best residual bulk flow, V_{ext} , that was fitted simultaneously with β^* using the Forward likelihood is also shown below. The bulk flow was computed by taking a $50 h^{-1}$ Mpc Gaussian-weighted mean of the velocity field corresponding to $\beta^* = 0.43$.

	v_x (km s $^{-1}$)	v_y (km s $^{-1}$)	v_z (km s $^{-1}$)	$\ v\ $ (km s $^{-1}$)	Longitude ($^\circ$)	Latitude ($^\circ$)
BF _{2M++}	-3 ± 8	-72 ± 11	38 ± 11	81 ± 11	268 ± 6	28 ± 10
LG _{2M++}	-18 ± 27	-422 ± 41	328 ± 37	535 ± 40	268 ± 4	38 ± 6
V_{ext}	89 ± 21	-131 ± 23	17 ± 26	159 ± 23	304 ± 11	6 ± 13
BF _{2M++} + V_{ext}	86 ± 22	-203 ± 26	55 ± 28	227 ± 25	293 ± 8	14 ± 10
LG _{2M++} + V_{ext}	71 ± 34	-553 ± 47	345 ± 46	656 ± 47	277 ± 4	32 ± 6

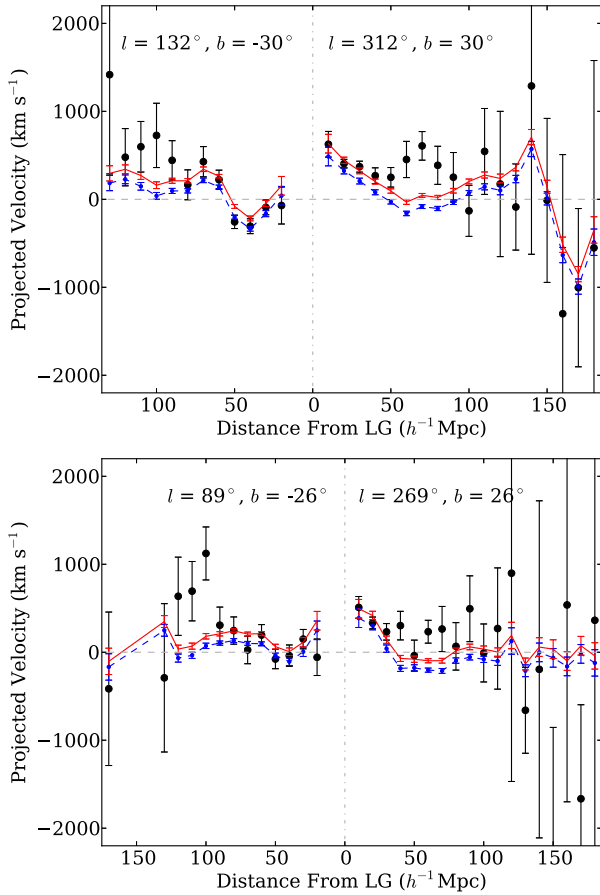


Figure 7. Measured velocities of objects from A1 and SFI++ lying within a 30° cone of Shapley/Great Attractor (upper), and Hydra Superclusters (lower). Velocities are projected on to the LOS. Predictions arising from 2M++ for our best value of $\beta^* = 0.43$ for these objects are shown above with and without the preferred residual bulk flow as connected blue dashed and red solid curves, respectively. Values plotted are the error weighted mean of velocities within bins of $10 h^{-1}$ Mpc. To the left of the origin the negative value of the peculiar velocity is plotted so that a bulk flow would appear as a constant offset.

apparent that predictions do in fact follow the trends observed in measured velocities. Furthermore, it is apparent that addition of V_{ext} to predicted velocities seems to provide better agreement, suggesting that such a residual bulk flow is in fact warranted.

In combination with a measurement of $\sigma_{8,g}^*$, β^* can be used to constrain the cosmology-dependent (and survey independent) degenerate parameter combination $f\sigma_8 = \beta^*\sigma_{8,g}^*$. To measure $\sigma_{8,g}^*$ from 2M++, we follow a similar prescription to that of Efstathiou et al. (1990), we compute $\sigma_{8,g}^* = \langle \sigma_{8,g}(r)/\psi(r) \rangle$ using counts in

cells within radial shells. Using this maximum likelihood scheme we obtain the value $\sigma_{8,g}^* = 0.99 \pm 0.04$, where the errors quoted are derived from the scatter among different shells, as this value was found to be more conservative than the formal errors from the likelihood analysis. This value is in good agreement with that found by Westover (2007) of $\sigma_{8,g}^* = 0.98 \pm 0.07$ obtained by fitting projected correlation functions to 2MRS galaxies within the magnitude range containing L^* galaxies, i.e. $-23.5 < K_s < -23.0$. The product of the growth factor and non-linear σ_8 is thus $f\sigma_8 = 0.427 \pm 0.026$. By adopting the value of $\Omega_m = 0.3$, we can transform our non-linear value of σ_8 to a linearized value following the prescription of Juszkiewicz et al. (2010). We in turn obtain the constraint $f\sigma_{8,\text{lin}} = 0.401 \pm 0.024$. It is important to note that linearization is only weakly dependent on the adopted value of Ω_m ($\Omega_m = 0.266$ results in $f\sigma_{8,\text{lin}} = 0.398 \pm 0.024$). We compare these results with those obtained using independent methods in the following section.

5 DISCUSSION

5.1 Potential systematic effects

In this section, we discuss the various effects which could bias our measurement of β^* and our prediction of the motion of the LG. Possible contributing factors include the following.

- (i) Choice of smoothing length used for Gaussian kernel may skew our estimate of β^* .
- (ii) Non-linear contributions to velocities from nearby small-scale structure may systematically bias results.
- (iii) Triple valued regions may result in incorrectly reconstructed galaxy positions skewing velocity predictions derived therefrom.
- (iv) As the reconstruction is being done in the LG frame, at each iteration we are subtracting the motion of the LG from all galaxies, our procedure may thus be susceptible to the Kaiser rocket effect.
- (v) Sparseness of survey may result in an under-representation of structures within the survey volume.
- (vi) Structures which lie in the ZoA are not included in 2M++ and could contribute to the direction and amplitude of the motion of the LG as well as influencing predictions of peculiar velocities of galaxies near the galactic plane.
- (vii) A non-linear relation between mass and luminosity as well as scatter in the underlying relation may influence predictions.

We have addressed some of these concerns above, but will review them again here for completeness.

In addressing (i), the width of the Gaussian kernel was chosen to be $4 h^{-1}$ Mpc as this length was shown to be least biased when velocity predictions were compared to those derived from simulations. Furthermore, this smoothing length was found to produce minimal scatter in the derived relation. We have accounted for (ii) and by performing the full reconstruction and analysis on data derived

from N -body simulations. It was found that a value of 150 km s^{-1} should be used for the scatter around predictions to account for these effects. As for (iii), we used maximum likelihood methods which integrate likelihoods along the LOS. As these methods account for uncertainty in a galaxy's position, results should not be sensitive to a misallocation of a galaxy in the event that it lies within a triple-valued region. The value of β^* derived from this analysis was found to be unbiased when performed on simulations. A more complete discussion of the quantification of these systematics through analysis of N -body simulations can be found in Appendix A.

As seen in Fig. 6, although the direction of the LG is not very susceptible to the value of β^* , the overall amplitude varies by $\sim 1200 \text{ km s}^{-1}$ between $\beta^* = 0$ and $\beta^* = 0.8$. As we are doing the reconstruction in the LG frame, an error in the estimate of the motion of the LG may result in spurious distance estimates of objects along this line of motion. Putting objects at the incorrect distance may in turn result in incorrect object weights, and in turn, incorrect velocity predictions. This phenomenon has come to be known as the Kaiser 'Rocket Effect', as it was first discussed in Kaiser (1987). To account for this effect, Strauss et al. (1992) explored a 'Kaiser Fix' to the *IRAS* 1.2 Jy sample. This 'fix' amounts to altering the predicted distances of objects to

$$r = cz - \hat{\mathbf{r}} \cdot (\mathbf{V}(r) - \mathbf{V}(0) \exp(-r^2/r_K^2)) - \mathbf{V}_{\text{CMB}} [1 - \exp(-r^2/r_K^2)], \quad (23)$$

where \mathbf{V}_{CMB} is the velocity of the LG as inferred from the CMB dipole, and where r_K is 1000 km s^{-1} as determined by the observed velocity correlation function (Bertschinger, Gorski & Dekel 1990). Note that this fix assumes that galaxies more distant than r_K are in fact at rest in the CMB frame, which may not be the case; indeed our data suggest otherwise. Nevertheless, to estimate the sensitivity of our results to this effect, we have implemented the Kaiser fix. We find that the final estimate of β^* differs by only 3 per cent, which is small compared to the random errors.

The impact of survey sparseness on the methodology applied in this work has been estimated in the past by Pike & Hudson (2005). For the 2MASS catalogue, they found that undersampling by 50 per cent produced negligible results on their final estimate of β^* (2–3 per cent). Furthermore, we have accounted for the effects of sparse sampling by obtaining our quoted results and errors from bootstrap resampling of both 2M++ and peculiar velocity data sets. In addressing (vi) we measured β^* at high latitudes ($b > 50^\circ$) and found no deviation from previous results beyond that of the random errors.

When the density field was normalized to the same bias, number-weighting and luminosity-weighting schemes yielded consistent results. As the χ^2 was found to be smaller for the luminosity weighted result than that obtained with number weighting, we hereafter will be quoting the best value of β^* as that obtained from the luminosity-weighting scheme. Results obtained in this paper account for neither a non-linear relation between mass and luminosity, nor do they account for scatter in mass–luminosity relation. More sophisticated models have been proposed, such as the halo-model of Marinoni & Hudson (2002), and recently an iterative prescription to reconstruct the density field from the distribution of haloes (Wang et al. 2009). We will consider implementation of such methods in a future paper.

5.2 Comparison with other results

As the bias depends on luminosity and possibly morphology (cf. Pike & Hudson 2005), the value of β obtained is survey dependent.

As 2M++ draws primarily from 2MASS, however, a loose comparison can be made with other values of β obtained therefrom. Most recently, in comparing the clustering dipole of galaxies from 2MASS-XSC to predictions from linear perturbation theory assuming a Λ CDM cosmology and convergence of the LG dipole with that derived from the CMB, Bilicki et al. (2011) found $\beta = 0.38 \pm 0.04$. After constructing β -dependent predictions of peculiar velocities, Branchini et al. (2012) in turn estimate β by minimizing the scatter of predicted 2MASS absolute magnitudes about a universal luminosity function and find $\beta = 0.323 \pm 0.083$. Davis et al. (2011) expand the velocity field in spherical harmonics and fit the inverse TF relation to SFI++ finding $\beta = 0.33 \pm 0.04$. The TF data span a range of distances, and because the effective bias changes with distance it is difficult to compare this directly with our number-weighted result $\beta^* = 0.44 \pm 0.02$. The characteristic, or error-weighted, depth of all individual SFI++ galaxies is $\sim 32 h^{-1} \text{ Mpc}$. At this distance, the typical relative bias of a number-weighted sample with the magnitude limit of 2MRS is $\psi_{2\text{MRS}}^N = b_{\text{eff}}/b_* = 0.93$, and so applying this to the Davis et al. (2011) result yields $\beta^* = 0.31 \pm 0.04$.

Our value of $f\sigma_{8, \text{lin}} = 0.40 \pm 0.02$ is in good agreement with those obtained using the same methodology, such as that of Turnbull et al. (2012) (0.40 ± 0.07), that of Pike & Hudson (2005) (0.44 ± 0.06), as well as with the weighted *IRAS* average of multiple studies reported therein (0.40 ± 0.03). As noted above, it is, however, in slight tension with that found by Davis et al. (2011) (0.31 ± 0.04). Note that where necessary the values quoted here have been linearized following the procedure discussed above in Section 4.3.

5.3 Cosmological implications

5.3.1 The value of $f\sigma_{8, \text{lin}}$

We can also compare our value $f\sigma_{8, \text{lin}}$ to constraints placed on a degenerate combination of Ω_m and σ_8 through independent means. In particular our value is in excellent agreement with a different peculiar velocity probe, namely measurements of $f(z)\sigma_8(z)$ at different redshifts via redshift space distortions, which yield a best-fitting value of $f\sigma_8 = 0.40 \pm 0.02$ (Hudson & Turnbull 2012).

An analysis of second- and third-order weak-lensing aperture-mass moments measured by CFHTLenS yields $\sigma_8(\Omega_m/0.27)^{0.6} = 0.79 \pm 0.03$ (Kilbinger et al. 2013). Constraints can also be obtained from the number counts and mass of galaxy clusters as measured through X-ray surface brightness (Vikhlinin et al. 2009) and measurements of the Sunyaev–Zeldovich (SZ) effect (Planck Collaboration XX 2014a, Reichardt et al. 2013). Finally, we can obtain a value for $f\sigma_8$ from CMB temperature anisotropy from *Planck* ($\Omega_m^{0.55}\sigma_8 = 0.427 \pm 0.010$; Planck Collaboration XIII 2015) and *WMAP9* ($\Omega_m^{0.55}\sigma_8 = 0.407 \pm 0.029$; Hinshaw et al. 2013). The measurements use different methods and are at different redshifts, and so their dependence on Ω_m differs in the exponent. To make a quantitative comparisons between different results, we adopt $\Omega_m = 0.3$ (see Fig. 8). There is some tension between some results e.g. Kilbinger et al. (2013) and Planck SZ (Planck Collaboration XX 2014a) versus *Planck* CMB temperature (Planck Collaboration XIII 2015). The peculiar velocity result presented here is consistent with all of these values.

5.3.2 The motion of the LG

For our best value of β^* we can compare the predicted growth of the LG velocity amplitude with the result that one would expect to

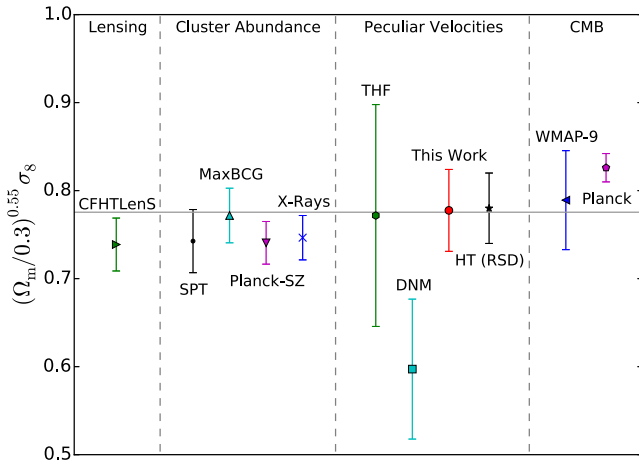


Figure 8. Comparison of $f\sigma_{8,\text{lin}}$ measured results. Values plotted above derived from weak-lensing (Kilbinger et al. 2013, CFHTLenS) and cluster abundances [Vikhlinin et al. (2009, X-rays); Rozo et al. (2010, MaxBCG); Planck Collaboration XX (2014a, Planck-SZ); Reichardt et al. (2013, SPT)] have assumed a value of $\Omega_m = 0.3$ in mapping constraints to $\Omega_m^{0.55}\sigma_8$. Results obtained through previous analyses of measured peculiar velocities are also shown [Davis et al. (2011, DNM); Turnbull et al. (2012, THF)], as well as from redshift space distortions (Hudson & Turnbull 2012, HT). CMB results are from WMAP9 and the Planck Collaboration XIII (2015). The horizontal line is the error-weighted mean of all values ($f\sigma_8 = 0.400 \pm 0.005$), shown here for reference.

measure using linear perturbation theory for a Λ CDM cosmology (conditional on V_{CMB}). For $\beta^* = 0.431 \pm 0.021$, as determined from peculiar velocity comparisons, we obtain the prediction for the motion of the LG arising from 2M++ to be $535 \pm 40 \text{ km s}^{-1}$ in the direction $l = 268^\circ \pm 4^\circ$, $b = 38^\circ \pm 6^\circ$, only 10° out of alignment with the direction of the motion as inferred from the CMB dipole. The residual LG motion is therefore $100 \pm 37 \text{ km s}^{-1}$ in the direction $l = 303^\circ \pm 36^\circ$, $b = 34^\circ \pm 36^\circ$. This value is in reasonable agreement with the best-fitting residual bulk flow obtained through peculiar velocity comparisons in the CMB frame of $159 \pm 23 \text{ km s}^{-1}$ in the direction $l = 304^\circ \pm 11^\circ$, $b = 6^\circ \pm 13^\circ$. Inclusion of this residual bulk flow with the predicted motion of the LG arising from 2M++ results in a total predicted motion of $656 \pm 47 \text{ km s}^{-1}$ in the direction $l = 277^\circ \pm 4^\circ$, $b = 32^\circ \pm 6^\circ$, in even better agreement with both the amplitude and direction of the motion as inferred from the temperature dipole of the CMB.

5.3.3 The residual bulk flow

We find that the amplitudes and directions of V_{ext} fit to each of the SFI++ and A1 SNe data sets separately are consistent with one another. Furthermore, comparing A1 with PSCz (of comparable depth to 2M++), Turnbull et al. (2012) found a residual flow of $V_x = 144 \pm 44 \text{ km s}^{-1}$, $V_y = -38 \pm 51 \text{ km s}^{-1}$, $V_z = 20 \pm 35 \text{ km s}^{-1}$, in reasonable agreement with the values found here of $V_x = 89 \pm 21 \text{ km s}^{-1}$, $V_y = -131 \pm 23 \text{ km s}^{-1}$, $V_z = 17 \pm 26 \text{ km s}^{-1}$. This suggests that the residual bulk flow is not an artefact of either the analysis or redshift-catalogue and is sourced by structures outside the 2M++ and PSCz volumes.

We can also use the 2M++ density field to predict the BF and compare this to the BF expected in a Λ CDM universe in Fig. 9. We have plotted this comparison for the Gaussian-weighted mean of the 2M++ velocity field. It is apparent from this figure that the resulting bulk flow from our analysis is in agreement with that expected for

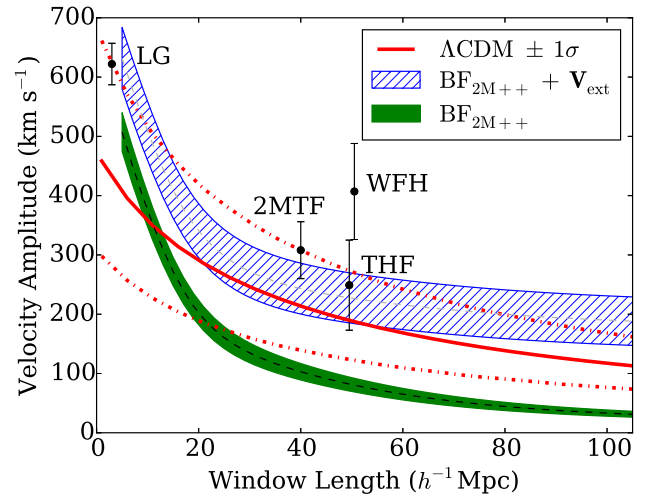


Figure 9. Volume-weighted mean of predicted velocity field for Gaussian window of increasing scale centred on the LG. The inferred values from 2M++ with and without the residual bulk flow are shown by the dashed grey line with 68 percent uncertainties in blue hatch, and a dashed black line, with uncertainties in solid green, respectively. The predicted root-mean-square velocity for a Λ CDM WMAP9 cosmology is shown as the red solid line, the cosmic scatter in the velocity amplitude distribution are shown as red dot-dashed lines. Bulk flows in Gaussian-weighted spheres of radius $40 h^{-1} \text{ Mpc}$ and $50 h^{-1} \text{ Mpc}$ are shown for the results of Hong et al. (2014, 2MTF), Turnbull et al. (2012, THF) and Watkins et al. (2009, WFH). The LG motion is also shown, plotted at a radius of $3 h^{-1} \text{ Mpc}$.

a Λ CDM universe. Combining the cosmic variance in quadrature with observational errors, comparison of the measured bulk flow of a $100 h^{-1} \text{ Mpc}$ Gaussian with predictions from Λ CDM yield a χ^2 of 1.4 for 3 degrees of freedom; clearly the measured value agrees well with the predicted value from the standard cosmological model.

5.3.4 A large-scale underdensity?

There have been recent claims that the Local Universe (~ 150 – $200 h^{-1} \text{ Mpc}$) is underdense (Keenan, Barger & Cowie 2013; Whitbourn & Shanks 2013). Such a phenomenon might account for the discrepancy between the larger value for the Hubble parameter when measured locally ($z \approx 0$) and that obtained from studies of the CMB temperature anisotropies.

Although the majority of 2M++ lies within the suggested underdensity, we have nonetheless explored the possibility of a underdense volume within 2M++. The luminosity-weighted density contrast of 2M++ in shells is shown in Fig. 10. We have not observed any global systematic rise in density towards the periphery of the survey.

To compare our results with others in more detail, note that Whitbourn & Shanks (2013) use redshift data from three large regions: 6dF-SGC, 6dF-NGC and SDSS-NGC. Within $z < 0.05$, they quote mean density contrast of $\bar{\delta}_g = -0.40 \pm 0.05$, 0.04 ± 0.10 and -0.14 ± 0.05 , respectively. For the same $z < 0.05$ volumes, we find density contrasts of $\bar{\delta}_* = -0.17$, 0.01 and 0.03 , respectively, where the density is normalized with respect to the mean density within $200 h^{-1} \text{ Mpc}$ ($z \sim 0.067$). Boehringer et al. (2015) studied the large-scale densities of X-ray clusters. For the 6dF-SGC and 6dF-NGC regions, they find mean cluster density contrast of $\bar{\delta}_{\text{cl}} = -0.55 \pm 0.10$ and 0.02 ± 0.17 within $z < 0.05$. However, as they point out, galaxy clusters are highly biased ($b_{\text{cl}} \sim 2.7$) and so the

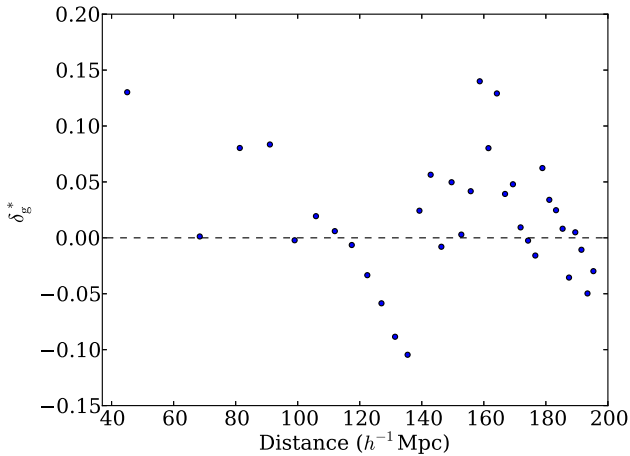


Figure 10. The mean density contrast of concentric spherical shells of equal volume centred on the LG.

corresponding mean matter density contrasts are $\bar{\delta}_m = -0.20 \pm 0.04$ and 0.01 ± 0.06 . These latter numbers are in good agreement with our nearly unbiased galaxy luminosity results. We conclude that, while the 6dF-SGC region may be mildly underdense within $z \lesssim 0.05$, there is no evidence for a large-scale void.

5.3.5 Prospects for the future

There are several upcoming peculiar velocity surveys which should dramatically improve the constraints on both β^* and $f\sigma_8$. Among these is the survey dubbed ‘Transforming Astronomical Imaging surveys through Polychromatic Analysis of Nebulae’ (TAIPAN). Using the UK Schmidt telescope, it is estimated that TAIPAN will acquire $\sim 45\,000$ Fundamental-plane velocity measurements out to a redshift of 0.2 (Koda et al. 2014). The next generation of TF peculiar velocity surveys include the Widefield ASKAP L-band Legacy All-sky Blind survey (WALLABY, Koribalski & Staveley-Smith 2009), and the Westerbork Northern Sky H I Survey (WNSHS).¹ An H I survey acquired using the Australian Square Kilometre Array Pathfinder (ASKAP), WALLABY is planned to cover 3π steradian of sky. Its Northern hemisphere counterpart, WNSHS, is planned to cover remaining π steradian of the sky using the Westerbork Synthesis Radio. It is estimated that these surveys will obtain a total of $\sim 32\,000$ velocity measurements, and along with TAIPAN will not only enable k -dependent measurements of $f\sigma_8$ but will improve constraints on this parameter combination at low redshift ($z \leq 0.05$) to within 3 percent (Koda et al. 2014). Clearly constraints on cosmology through peculiar velocities have a very promising future.

6 CONCLUSION

Under the assumption of gravitational instability, we reconstructed the galaxy density field within $200\,h^{-1}$ Mpc using 2M++, a composite all-sky redshift survey with high completeness. We compared the predicted peculiar velocities arising from this density field to the measured peculiar velocities of SFI++ and the First Amendment supernovae data set using various comparison methods in order to measure $\beta^* = \Omega_m^{0.55}/b^*$. Using the VELMOD maximum likelihood

comparison method with SFI++ spiral galaxies, we simultaneously solved for the inverse TF relation zero-point and slope, β^* , as well as a residual bulk flow due to sources external to the 2M++ volume, denoted V_{ext} . We similarly compared peculiar velocities data sets to predictions from 2M++ using a forward-likelihood method in order to constrain β^* and V_{ext} . All methods and data subsets yielded consistent values of β^* , with our final result being $\beta^* = f(\Omega_m)/b^* = 0.431 \pm 0.021$. Combining our value of β^* with $\sigma_{8,\text{gal}}^* = 0.99 \pm 0.04$ as measured from 2M++ for $\beta^* = 0.43$, we in turn measured the parameter combination $f\sigma_{8,\text{lin}} = 0.401 \pm 0.024$. This value was found to be consistent with the majority of results obtained by independent means, including those of WMAP9 and Planck.

For our measured value of β^* , we computed the velocity of the LG as predicted by linear perturbation theory arising from the reconstructed density field. Our value for the velocity was found to be consistent with the theoretical value that would be measured for a survey of this depth in a Λ CDM Universe. Combining our predicted value for the motion of LG arising from 2M++ for our best value of β^* with the value of V_{ext} obtained through comparing predicted velocities with peculiar-velocity surveys, we predict a motion of the LG to be $660 \pm 50\,\text{km s}^{-1}$, towards $l = 277^\circ \pm 4^\circ$, $b = 32^\circ \pm 6^\circ$, only 5° out of alignment with the direction as inferred from the CMB dipole. Similarly, with addition of this residual bulk flow to the $50\,h^{-1}$ Mpc Gaussian-weighted mean of the velocity field, we obtained a predicted bulk-flow of $230 \pm 30\,\text{km s}^{-1}$ towards $l = 293^\circ \pm 8^\circ$, $b = 14^\circ \pm 10^\circ$, an amplitude that is consistent with that expected for a Λ CDM Universe. We note, however, that although we find the inclusion of V_{ext} is preferred at the 5.1σ level, it is unclear whether this residual bulk flow merely compensates for imperfect mapping between luminosity and mass towards the periphery of 2M++, or whether it is due to structures outside the 2M++ volume. Future work using more sophisticated biasing schemes may help in answering this question.

The resulting 2M++ density and peculiar velocity fields obtained from this analysis are made available at cosmicflows.uwaterloo.ca and cosmicflows.iap.fr.

ACKNOWLEDGEMENTS

All authors acknowledge support from the Natural Sciences and Engineering Council of Canada. This work made in the ILPLABEX (under reference ANR-10-LABX-63) was supported by French state funds managed by the ANR within the Investissements d’Avenir programme under reference ANR-11-IDEX-0004-02.

REFERENCES

- Abazajian K. N. et al., 2009, *ApJS*, 182, 543
- Behroozi P. S., Wechsler R. H., Wu H.-Y., 2013, *ApJ*, 762, 109
- Berlind A. A., Narayanan V. K., Weinberg D. H., 2000, *ApJ*, 537, 537
- Bertschinger E., Gorski K. M., Dekel A., 1990, *Nature*, 345, 507
- Bilicki M., Chodorowski M., Mamon G. A., Jarrett T., 2011, *ApJ*, 741, 31
- Bilicki M., Chodorowski M., Jarrett T., Mamon G. A., 2011, *ApJ*, 741, 31
- Blanton M. R. et al., 2005, *AJ*, 129, 2562
- Boehringer H., Chon G., Bristow M., Collins C. A., 2015, *A&A*, 574, 26
- Branchini E., Davis M., Nusser A., 2012, *MNRAS*, 424, 472
- Courteau S., van den Bergh S., 1999, *AJ*, 118, 337
- Davis M., Huchra J., 1982, *ApJ*, 254, 437
- Davis M., Nusser A., Masters K. L., Springob C., Huchra J. P., Lemson G., 2011, *MNRAS*, 413, 2906
- Efstathiou G., Kaiser N., Saunders W., Lawrence A., Rowan-Robinson M., Ellis R. S., Frenk C. S., 1990, *MNRAS*, 247, 10p

¹ <http://www.astron.nl/~jozsa/wnsht/>

- Erdođdu P. et al., 2006a, MNRAS, 368, 1515
 Erdođdu P. et al., 2006b, MNRAS, 373, 45
 Folatelli G., Phillips M. M., Burns C. R., Contreras C., 2010, AJ, 139, 120
 Hicken M., Wood-Vasey W. M., Blondin S., Challis P., Jha S., Kelly P. L., Rest A., Kirshner R. P., 2009, ApJ, 700, 1097
 Hinshaw G. et al., 2009, ApJS, 180, 225
 Hinshaw G. et al., 2013, ApJS, 208, 19
 Hong T. et al., 2014, MNRAS, 445, 402
 Huchra J. P., Geller M. J., 1982, ApJ, 257, 423
 Huchra J. P. et al., 2012, ApJS, 199, 26
 Hudson M. J., Turnbull S. J., 2012, ApJ, 751, L30
 Jha S., Riess A. G., Kirshner R. P., 2007, ApJ, 659, 122
 Jones D. H. et al., 2009, MNRAS, 399, 683
 Juszkiewicz R., Feldman H. A., Fry J. N., Jaffe A. H., 2010, J. Cosmol. Astropart. Phys., 2, 21
 Kaiser N., 1987, MNRAS, 227, 1
 Keenan R. C., Barger A. J., Cowie L. L., 2013, ApJ, 775, 62
 Kilbinger M., Fu L., Heymans C., Simpson F., Benjamin J., Erben T., Harnois-Deraps, 2013, MNRAS, 430, 735
 Koda J. et al., 2014, MNRAS, 445, 4267
 Koribalski B., Staveley-Smith L., 2009, ASKAP Survey Science Proposal, available online at: <http://www.atnf.csiro.au/research/WALLABY/proposal.html>
 Lahav O., Kaiser N., Hoffman Y., 1990, ApJ, 352, 448
 Lavaux G., Hudson M. J., 2011, MNRAS, 416, 2840
 Lavaux G., Tully R. B., Mohayaee R., Colombi S., 2010, ApJ, 709, 483
 Marinoni C., Hudson M. J., 2002, ApJ, 569, 101
 Masters K. L., Springob C. M., Haynes M. P., Giovanelli R., 2006, ApJ, 653, 861
 Norberg P. et al., 2001, MNRAS, 328, 64
 Peebles P. J. E., 1993, Principles of Physical Cosmology. Princeton Univ. Press, Princeton, NJ
 Pike R. W., Hudson M. J., 2005, ApJ, 635, 11
 Planck Collaboration XX, 2014a, A&A, 571, A20
 Planck Collaboration XXVII, 2014b, A&A, 571, A27
 Planck Collaboration XIII, 2015, A&A, Submitted
 Reichardt C. L. et al., 2013, ApJ, 763, 127
 Rozo E. et al., 2010, ApJ, 708, 645
 Saunders W. et al., 2000, MNRAS, 317, 55
 Schechter P., 1976, ApJ, 203, 297
 Skrutskie M. F. et al., 2006, AJ, 131, 1163
 Springel V., 2005, MNRAS, 364, 1105
 Springob C. M., Masters K. L., Haynes M. P., Giovanelli R., Marinoni C., 2007, ApJS, 172, 599
 Strauss M. A., Yahil A., Davis M., Huchra J. P., Fisher K., 1992, ApJ, 397, 395
 Tegmark M., Dodelson S., Eisenstein D. J., Narayanan V., 2002, ApJ, 571, 191
 Turnbull S. J., Hudson M. J., Feldman H. A., Hicken M., Kirshner R. P., Watkins R., 2012, MNRAS, 420, 447
 Vikhlinin A. et al., 2009, ApJ, 692, 1060
 Wang L., Steinhardt P. J., 1998, ApJ, 508, 483
 Wang H., Mo H. J., Jing Y. P., Guo Y., van den Bosch F. C., Yang X., 2009, MNRAS, 394, 398
 Watkins R., Feldman H. A., Hudson M. J., 2009, MNRAS, 392, 743
 Westover M., 2007, PhD dissertation, Harvard University
 Whitbourn J. R., Shanks T., 2013, MNRAS
 Willick J. A., Strauss M. A., 1998, ApJ, 507, 64
 Willick J. A., Strauss M. A., Dekel A., Kolatt T., 1997, ApJ, 486, 629
 Yahil A., Strauss M. A., Davis M., Huchra J. P., 1991, ApJ, 372, 380

APPENDIX A: TESTS OF THE RECONSTRUCTION WITH *N*-BODY SIMULATIONS

In this Appendix, we focus on two possible sources of systematic bias in the reconstructed density and velocity fields. First, when

constructing the density field from a set of point density tracers, it is necessary to smooth to obtain a continuous density field. If the smoothing length is too short, density contrasts are high and linear perturbation theory is no longer applicable. If the smoothing length is too long, then the density contrast is suppressed and velocities are underpredicted. Secondly, in ‘reconstructing’ real-space positions from redshift-space, the iterative technique discussed in Section 3 may also introduce a systematic bias in the recovered density field and hence in the fitted value of β .

A1 Effect of smoothing

Berlind, Narayanan & Weinberg (2000) used *N*-body simulations to show that when predicted velocities derived from smooth density fields are compared to measured (unsmoothed) velocities, the recovered value of β depends on the smoothing. For Gaussian smoothing, unbiased results were obtained for a smoothing radius between 4 and 5 h^{-1} Mpc. It is interesting to confirm these results.

Here we use an *N*-body simulation of 512^3 particles in a $500 h^{-1}$ Mpc periodic box using GADGET-2 (Springel 2005). The cosmological parameters of this simulation are as follows: $\Omega_m = 0.266$, $\Omega_\Lambda = 0.734$, $h = 0.71$, and where each particle is $6.83 \times 10^{10} h^{-1} M_\odot$. From the particle positions and velocities of the simulation, a halo catalogue was formed using ROCKSTAR (Behroozi, Wechsler & Wu 2013) consisting of 693 948 haloes between 5.5×10^{11} and $2.2 \times 10^{15} h^{-1} M_\odot$ (between 8 and 31 809 particles). Either halo or particle positions were smoothed to create a smooth halo or particle density field.

In Fig. A1, we plot both the slope of regression between smoothed predicted and *N*-body velocities, as well as the scatter about this relation, both as a function of smoothing scale.

For particle velocities compared with the linear theory predictions from the smoothed particle density field, the slope is unbiased at a smoothing scale of $\sim 5 h^{-1}$ Mpc. The scatter is $\sim 250 \text{ km s}^{-1}$. The results are similar for haloes, but the scatter is significantly lower: $\sim 150 \text{ km s}^{-1}$. This is because the particle velocity field is a sum of the motion of the haloes themselves plus the internal motion of particles with respect to the haloes. In both cases, the scatter is minimum for a smoothing scale of $\sim 4 h^{-1}$ Mpc.

A2 Reconstructing the halo distances from redshifts

With actual galaxy data, the true distances are unknown but redshifts are available. In this paper, we use an iterative reconstruction method to map a galaxy’s position from redshift space to real space. We will refer to these reconstructed coordinates as ‘recon-space’. In the *N*-body simulation, we emulate this by placing haloes in redshift-space, and then iteratively reconstruct the density field, slowly increasing β .

Fig. A2 shows the difference between real-space positions and recon-space positions. The left-hand panel illustrates the absolute displacement in units of km s^{-1} . From this panel, it is apparent that in recon-space the majority of haloes do in fact return to a location close to their real-space positions, with an error that is typically $\sim 300 \text{ km s}^{-1}$. This is smaller than the smoothing scale of $\sim 4 h^{-1}$ Mpc. However, in practice this reconstruction error will act as an additional source of smoothing. We will return to this point below.

The right-hand panel shows the displacement of each halo from its real-space position normalized by the difference between the real-space and redshift-space positions (i.e. by their peculiar velocities). In this way, the haloes which lie in redshift-space have a

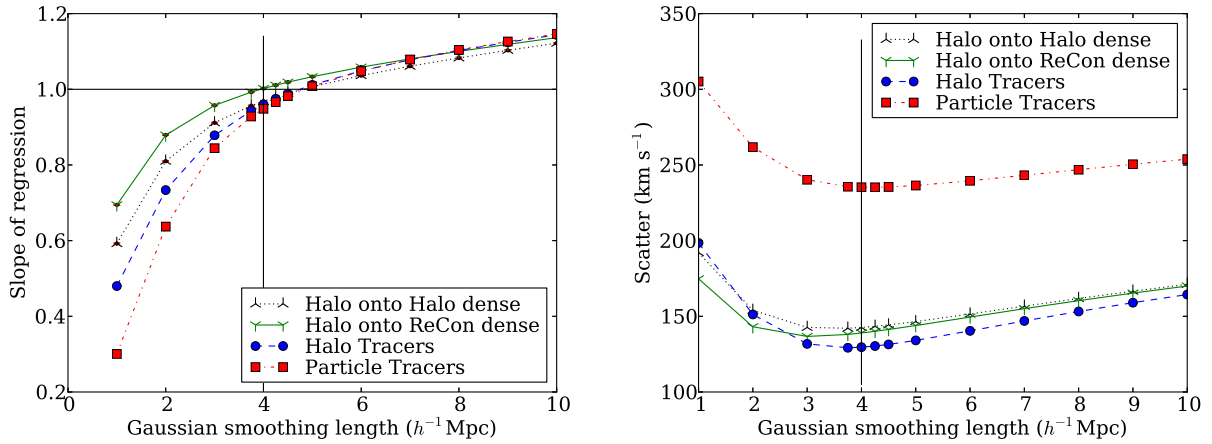


Figure A1. The fitted slope of the regression between N -body observed peculiar velocities and the linear theory predictions as a function of smoothing scale is shown in the left-hand panel. In the right-hand panel, the scatter about the same regression is plotted. Either particles or haloes can be used as tracers of the density field, or as tracers of the velocity field. The blue circles and red squares represent halo tracers and particle tracers, respectively. The black curve with downwards pointing 'Y' show the resulting scatter when the known halo velocities are compared to the predictions from the halo density field. The green curve with 'Y'-shaped symbols show the resulting scatter when the known halo velocities are compared to the predictions from the reconstructed halo density field. Note that the reconstruction process shows very nearly unbiased results when the field is smoothed with a Gaussian kernel that is $4 h^{-1}$ Mpc in length.

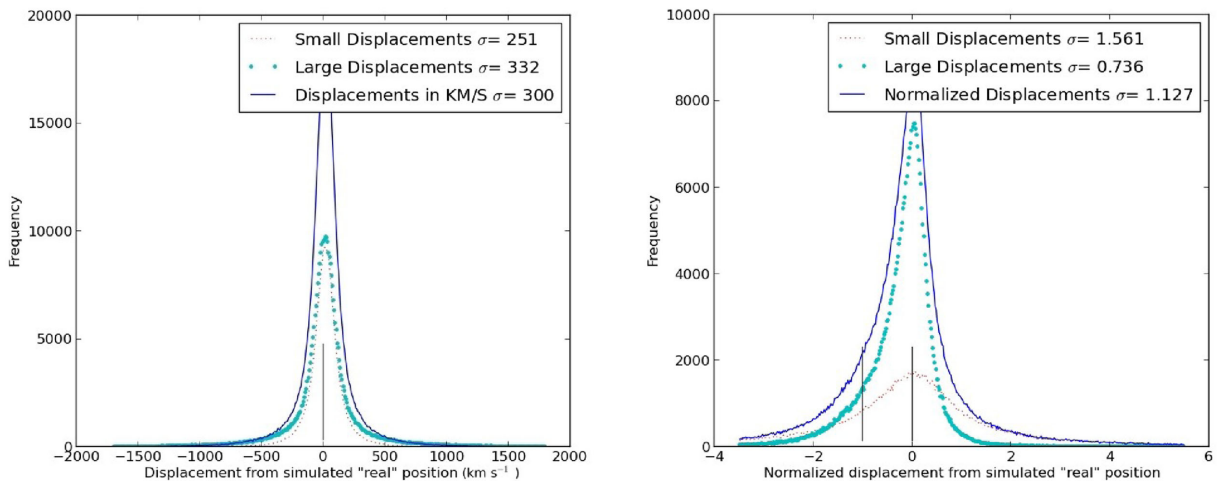


Figure A2. Two sample histograms showing the relative displacement of haloes in recon-space to their real-space positions. The recon-space positions used are those which correspond to the number of iterations required to recover the known value of β . The left-hand panel illustrates the absolute displacement in km s^{-1} , whereas the right-hand panel shows the displacement of haloes normalized by the difference between real-space and redshift-space positions. As such, a normalized displacement of -1 corresponds to a halo lying at its redshift-space position, and a normalized displacement of 0 corresponds to a halo returning to its real-space position. The solid blue curve corresponds to all haloes, the turquoise dotted curve corresponds to haloes with known velocities greater than 150 km s^{-1} , and the dotted red curve corresponds to haloes with known velocities less than 150 km s^{-1} . Haloes which have a normalized displacement less than -1 have moved away from their initial positions due to lying within triple-valued regions. Haloes which have a normalized displacement greater than 0 have moved to their initial positions and beyond.

normalized displacement of -1 , and those which have returned to real-space have a normalized displacement of 0 . With each successive iteration, tracers would all ideally return to 0 , i.e. return to the position they had in real-space. Haloes which have a normalized displacement more negative than -1 have moved away from their initial positions. We argue below (Section B) that these are haloes in triple-valued regions. From this figure, it can be seen that the typical tracer does in fact return to its real-space position. However, the distinction between low and high peculiar velocity tracers is more pronounced. The tracers with a low peculiar velocity have a symmetric distribution of reconstruction error. The haloes which initially have a high velocity, however, have a more skewed distribution which likely results in part from triple-valued regions.

Having reconstructed the density field in recon-space, we return to the question of how well this field, once smoothed, can predict peculiar velocities. Fig. A1 shows the results of this comparison. The fitted slope obtained from the reconstructed density field is systematically offset in comparison to those obtained from the real-space halo density field. The key result is that predicted velocities derived from the reconstructed smoothed halo fields yields an unbiased value of the slope, i.e. β , when a Gaussian kernel of $4 h^{-1}$ Mpc is used. This value is smaller than the value of $\sim 5 h^{-1}$ Mpc found for haloes in real-space, because the recon-space density field is effectively pre-smoothed (in the redshift direction) by the $\sim 300 \text{ km s}^{-1}$ reconstruction error discussed above.

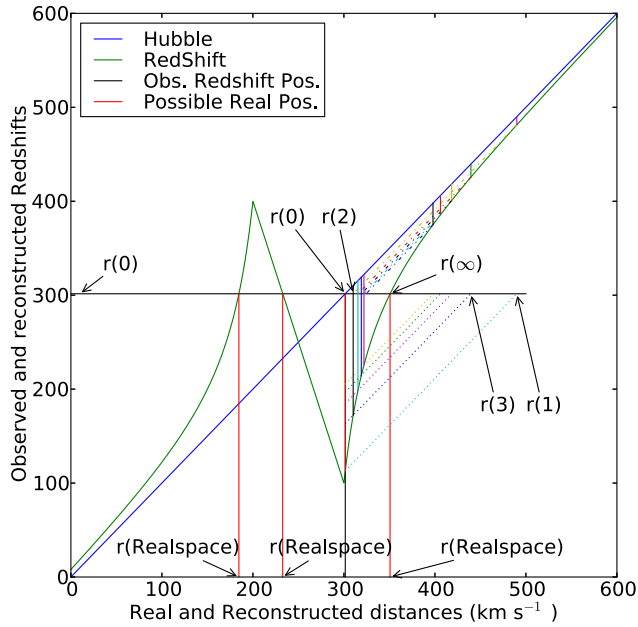


Figure B1. Simplified reconstruction of one test object near a fixed potential well. In a Universe without structure, Hubble’s law (blue solid line $y = x$) would be sufficient to convert from redshift to real-space positions. In a Universe containing a spherical top-hat overdensity, however, the relation is complicated by infall towards the well (green solid curve). An object with an observed redshift in excess of 300 km s^{-1} can be seen to have originated from three possible real-space positions (vertical red solid lines). The reconstruction process starts by placing the particle at its observed redshift, predicting its velocity, and then subtracting that prediction from the original observation (the dotted lines parallel to the Hubble law line) to get a new predicted position. In most situations this new position will be beyond one of the possible real-space positions where the predicted infall velocities are small. Repeating the process here results in a much smaller velocity offset which can be projected (dot-dashed lines) back to the observed velocity to find the next reconstructed position. The iterative reconstruction converges in most situations to one of the two outer possible real-space positions. Reconstructed positions never converge, however, to the central possible real-space position.

APPENDIX B: ITERATIVE RECONSTRUCTION NEAR TRIPLE-VALUED REGIONS

One problem with any reconstruction method is correcting for the fact that mapping from redshift to position is multivalued, i.e. there can be several distances which map to the same redshift.

To give an illustration as to how this affects the iterative reconstruction method, we have created a simple toy model in Fig. B1 which shows the velocity field around a spherical overdensity. One can see that for any object with an observed redshift in the range ~ 100 to $\sim 400 \text{ km s}^{-1}$, there are multiple distances that correspond

to that given redshift. As a concrete example, consider a galaxy at a redshift of 300 km s^{-1} . We will consider a simplified version of our reconstruction scheme in order to illustrate the general behaviour. In this simplified version, the value of β is held fixed, i.e. it is not increased adiabatically, so the amplitude of the peculiar velocity curve is fixed and the curve $cz(r)$ is also fixed.

In the first step of this iterative process, we place the galaxy at a distance corresponding to its observed redshift: 300 km s^{-1} at position $r(0)$ in Fig. B1. At this location, the predicted peculiar velocity is approximately -190 km s^{-1} , so the object is moved to its first reconstructed position of $490 \text{ km s}^{-1} = 300 \text{ km s}^{-1} - (-190 \text{ km s}^{-1})$ at position $r(1)$. At this position, it has a predicted peculiar velocity of approximately -20 km s^{-1} , and so this predicted peculiar velocity is again subtracted from its observed redshift of 300 km s^{-1} , resulting in a reconstructed distance of 320 km s^{-1} indicated $r(2)$. In this example, each successive loop brings the reconstructed position closer to the outer redshift solution of approximately 360 km s^{-1} indicated $r(\infty)$. The same behaviour occurs for redshifts between 250 and 400 km s^{-1} , the final position converges to the third (outer) of the three values. For redshifts between 100 and 250 km s^{-1} , in contrast, the recon position converges to the first of the three values. One can see that the outer solutions are attractors, and the middle solution is unstable.

The above toy model is for a test particle (e.g. galaxy) moving in a fixed potential well (e.g. supercluster). It can also happen that two similar-mass galaxies (or two clusters) may each respond to the other’s gravity. In this situation, the distances of the two objects can ‘leapfrog’, i.e. can exchange the order of their distances in reconstructed space. This leads to a sign change of the predicted peculiar velocity, which then leads to another ‘leapfrog’ and a subsequent sign change in predicted peculiar velocity. Hence some objects show oscillatory behaviour in the reconstructed distance.

Note however that the simple model described above and in Fig. B1 is an oversimplification of our reconstruction process. Of course, while in reality the density field used is a smoothed Gaussian random sphere not a spherical top-hat overdensity, qualitatively the behaviour around overdensities is similar. More importantly, our iterative scheme is more complex than the one outlined above. First, we ‘adiabatically’ increase β^* at each iteration. Consequently, the amplitude of the predicted peculiar velocity field increase slowly and so the size of triple-valued regions in redshifts space grows slowly. Secondly, we reduce oscillatory behaviour by averaging the positions of several successive iterations. Thus, the convergence is better-behaved than the toy model described above. But qualitatively, the effect remains the same: as a result of preferentially placing objects towards the periphery of triple-value regions, the density field is effectively ‘smoothed’ more in the regions of highest density.

This paper has been typeset from a \LaTeX file prepared by the author.